

Plasma parameters and tungsten sputter rates in a high-frequency CCP


Cite as: Phys. Plasmas **29**, 043511 (2022); <https://doi.org/10.1063/5.0083613>

Submitted: 28 December 2021 • Accepted: 13 March 2022 • Published Online: 13 April 2022

 M. Sackers,  C. Busch,  Ts. V. Tsankov, et al.

COLLECTIONS

 This paper was selected as Featured

 This paper was selected as Scilight



View Online



Export Citation



CrossMark

ARTICLES YOU MAY BE INTERESTED IN

[Sudden collapse of a pressure profile generated by off-axis heating in a linear magnetized plasma](#)

Physics of Plasmas **29**, 042104 (2022); <https://doi.org/10.1063/5.0082247>

[Laser-driven, ion-scale magnetospheres in laboratory plasmas. I. Experimental platform and first results](#)

Physics of Plasmas **29**, 042901 (2022); <https://doi.org/10.1063/5.0084353>

[High-speed imaging of magnetized plasmas: When electron temperature matters](#)

Physics of Plasmas **29**, 032104 (2022); <https://doi.org/10.1063/5.0083130>



Physics of Plasmas
Features in Plasma Physics Webinars

Register Today!



Plasma parameters and tungsten sputter rates in a high-frequency CCP

Cite as: Phys. Plasmas **29**, 043511 (2022); doi: [10.1063/5.0083613](https://doi.org/10.1063/5.0083613)

Submitted: 28 December 2021 · Accepted: 13 March 2022 ·

Published Online: 13 April 2022



View Online



Export Citation



CrossMark

M. Sackers,^{1,a)}  C. Busch,²  Ts. V. Tsankov,²  U. Czarnetzki,²  Ph. Mertens,¹  and O. Marchuk¹ 

AFFILIATIONS

¹Forschungszentrum Jülich GmbH, Institut für Energie- und Klimaforschung – Plasmaphysik, Partner of the Trilateral Euregio Cluster (TEC), 52425 Jülich, Germany

²Institute for Plasma and Atomic Physics, Faculty of Physics and Astronomy, Ruhr University Bochum, D-44801 Bochum, Germany

^{a)} Author to whom correspondence should be addressed: m.sackers@fz-juelich.de

ABSTRACT

Monitoring and investigating the fusion plasma in ITER will be crucial to pave the way to a fusion power plant. However, the harsh conditions in the vacuum vessel are detrimental for the optical diagnostics systems. Replacing the element with a direct line of sight to the fusion plasma by a metallic mirror shifts the problem to this component. The flux of impurities onto these mirrors accumulate to deposits, which degrade their optical properties over time. It has been proposed to address this issue by igniting discharges in front of the mirrors during the maintenance phases allowing the deposited material to be sputtered away and recover the mirror properties. To further the knowledge for such an option, in this work, plasma parameters and sputter rates in a high-frequency (60 MHz) capacitive discharge in argon at pressures below 10 Pa are studied. The powered electrode consists of tungsten as a cheap rhodium proxy—the material of the metallic mirrors in ITER—and to simulate tungsten deposition. Its size is equivalent to a mirror for charge-exchange recombination spectroscopy at ITER (8.5 cm × 18 cm). The discharge is studied using and interpreting voltage measurements, microwave interferometry, electrical probe measurements, and optical emission spectroscopy. These investigations provide the opportunity to identify the optimal conditions for the process based on various requirements, such as damage threshold of the mirror crystal and severity and type of contamination.

© 2022 Author(s). All article content, except where otherwise noted, is licensed under a Creative Commons Attribution (CC BY) license (<http://creativecommons.org/licenses/by/4.0/>). <https://doi.org/10.1063/5.0083613>

I. INTRODUCTION

Optical diagnostics will play a crucial role at the ITER experiment to understand the underlying physics and of the performance of the fusion reactor.^{1–3} A direct line of sight of the detectors to the fusion plasma is undesirable due to the high magnetic field strength, irradiation damage by fusion neutrals, and deposition of sputtered wall material that can degrade their performance. Instead, a series of mirrors starting with metallic first mirrors (FMs) are envisioned to address this issue.

It is anticipated that plasma–surface interactions will lead to significant sputtering of the first wall material (beryllium⁴) of the divertor plates (tungsten⁵) and of other exposed metallic components.⁶ The sputtered material will then be transported and deposited elsewhere in the chamber, including the first mirrors of the various diagnostic systems. These depositions might drastically alter the reflectivity of the FMs,^{3,7,8} which will pose difficulties for the interpretation of the measured light signals. Thus, it is necessary to remove the accumulated depositions during the maintenance phases. One possibility is to take

out the mirrors and clean them outside. However, this would require venting the vacuum vessel to allow the removal of the mirrors. Not surprisingly, such a solution is highly undesirable due to the difficult access to the vacuum chamber, the expected contamination with radioactive materials from the bombardment with fusion neutrons, and prolonging of the maintenance phases to potentially unacceptable levels. Evidently, a remote, *in situ*, and *in vacuo* cleaning method would avoid these issues and is, thus, an enticing option. One way for achieving this is by igniting a discharge that uses the conductive mirrors as electrodes, which will be able to clean away the accumulated coatings and to recover the mirror properties. A DC or an RF discharge are two possible options commonly used for sputtering of surface materials.

The first challenge is that an anticipated contaminant is beryllium, a well-known oxygen retainer.⁹ Consequently, the non-conductive BeO ceramic is an expected predominant coating. The presence of an insulating layer on the electrodes leads to charging up of the surface and renders the option of using a DC discharge

unfeasible. RF discharges do not suffer from this problem due to the alternating voltage that is applied. This motivates their application as a method for cleaning the metal first mirrors in ITER. From the various types of RF plasmas, probably the ones best suited for this purpose are the capacitive discharges.¹⁰ First experimental campaigns using capacitive RF discharges at various frequencies (13.56 MHz,^{11–14} 60 MHz,¹⁵ 81.36 MHz^{11,16}) aiming to remove coatings from metallic mirrors, were conducted recently. The choice of these frequencies is not arbitrary. On the one hand, these are standard frequencies used in industrial applications, and the equipment is readily available and easy to obtain.¹⁷ On the other hand, these frequencies lie outside the frequency range of 40–55 MHz, reserved in ITER for use by the ion cyclotron resonant heating system.¹⁸ Higher frequencies produce plasmas with higher density and lower sheath voltages, i.e., lower ion impact energies.¹⁰ However, driving the discharge at higher frequencies poses a challenge in delivering the power to the metallic mirror without losses in the transmission lines and decreases the homogeneity of the cleaning process.¹⁹ The frequency of 60 MHz appears as a good compromise in this regard and is chosen for the present studies.

The previous studies verified that a robust operation of an RF cleaning discharge is possible. Aluminum coatings were successfully removed from a molybdenum mirror restoring its spectral reflectivity.^{13,15} To further clarify the sputtering mechanisms, Razdobarin *et al.*¹¹ investigated the ion impact energy in a neon and deuterium discharge by a retarding field analyzer and simulated the plasma parameters with the CFD-ACE+ software. They reported that indeed coatings of Al and Al₂O₃, used as Be and BeO proxies, were removed from a polycrystalline molybdenum mirror using an RF discharge. In their work, a magnetic field normal to the mirror surface was generated that significantly improved the homogeneity of the cleaning process and reduced the sputter rate. Measurements by Moser *et al.*¹² using an argon discharge in the presence of a magnetic field support these findings. Very recently, a cleaning discharge was investigated in the EAST tokamak by Yan *et al.*¹⁴ These authors showed homogeneous removal of Al₂O₃ from a molybdenum mirror in the presence of the 1.7 T-strong toroidal magnetic field of the tokamak. Dmitriev *et al.*¹⁶ extended the analysis to a removal of Al and Al₂O₃ coatings from a stainless steel electrode by bombardment with 100 eV neon ions.

Most of these studies concentrated on the use of capacitive discharges in neon or Ne/D₂ mixtures. On the other hand, argon shows similar or even larger sputter rates compared to neon.¹³ Furthermore, its lower ionization energy leads to higher plasma density and, hence, to higher ion fluxes and faster sputtering. In capacitive discharges, the higher plasma density correlates with lower sheath voltages,¹⁰ i.e., lower ion impact energies, which would be beneficial for preventing damage to the mirror.

At present, it is unclear if a substantial amount of tungsten will be accumulated on the mirrors. Codes for plasma impurity transport, such as a combination of SolEdge2D-EIRENE²⁰ and ERO2.0,^{21,22} will give an estimate of the expected depositions. Regardless of the result, it is important to understand if contamination with tungsten can be handled. Pure deuterium discharges cannot remove tungsten atoms at an acceptable rate due to the large mass difference. Heavier ion species would provide efficient sputtering of tungsten, but this would come at the cost of risking sputtering also of the mirror material. Some experimental data on a suitable operation regime exist already. For example,

Mertens *et al.*³ exposed a rhodium mirror to an Ar–H plasma at the linear plasma device PSI-2²³ for 75 min. The mirror was biased so that the bombarding ions were nearly mono-energetic with an impact energy of 100 eV. These authors reported that the optical properties of the mirror did not deteriorate. However, this may not remain valid at higher impact energies.

In this work, we investigate a capacitively coupled plasma (CCP) at 60 MHz operated in argon. The powered electrode has the dimensions of the first mirror for the core charge exchange recombination spectroscopy (CXRS) system at ITER (8.5 cm × 18 cm)³ and is made of tungsten. This choice of material serves two purposes. On the one hand, tungsten will probably be the most challenging deposition to be removed. It is then important to understand the plasma conditions that would facilitate that. These conditions will probably be suitable also for the removal of the other expected depositions. On the other hand, tungsten has similar sputtering characteristics to rhodium, the material of the actual CXRS mirrors. These studies then indicate the plasma conditions needed to avoid damage to the mirror crystal. The studies concentrate on pressures below 10 Pa and impact energies of around 100 eV. These energies are possible due to the large geometrical asymmetry of the plasma vessel, leading to large self-bias of the driven electrode.

The different aspects of the sputtering of the electrode material are investigated by a combination of diagnostic methods. Microwave interferometry combined with a movable Langmuir probe yield the radial profiles of the electron density and an estimation of the electron temperature. Optical emission spectra are analyzed using a collisional-radiative model, which provides benchmark values for these plasma parameters and spatial resolution in the vertical direction. The impact energy of the ions is derived from voltage measurements. This allows the sputter rate caused by the bombarding argon ions to be estimated using the empirical formula for the sputter yield by Eckstein and Preuss.^{24–26} The sputter rates obtained at different discharge conditions are correlated with the intensity of selected tungsten lines. The excellent agreement between these methods shows the consistency of the obtained sputter rates permitting an estimation of the optimal discharge conditions.

The paper is structured as follows. First, the experimental setup is described in Sec. II. Section III presents the results for the plasma parameters—electron density and temperature, as well as the energy of the impinging ions—together with the way they are obtained. In Sec. IV, these parameters are used to deduce and analyze the sputter rates of the tungsten electrode. Section VI wraps up the findings at the end.

II. EXPERIMENTAL SETUP AND DIAGNOSTICS

A. Discharge chamber

The investigations are performed in a capacitively coupled discharge (CCP) in argon. The discharge is ignited in a cylindrical vessel, 2R = 90 cm in a diameter and a height of H = 90 cm (Fig. 1). A turbomolecular pump (TURBOVAC MAG W 600 P, Leybold) in a combination with an oil-free pump (Ecodry M15, Leybold Vacuum) provides a base pressure of 1×10^{-4} Pa. A mass flow controller (MF1 100 SCCM, MKS) regulates the flow of argon into the vessel. The working pressure is regulated by adjusting the gas flow rate and the position of a gate valve in front of the turbomolecular pump. The position of the gate valve (SH8618M5304-KVA2, Nanotec) is set by a controller (PM-5, VAT) that receives a feedback signal from a capacitive

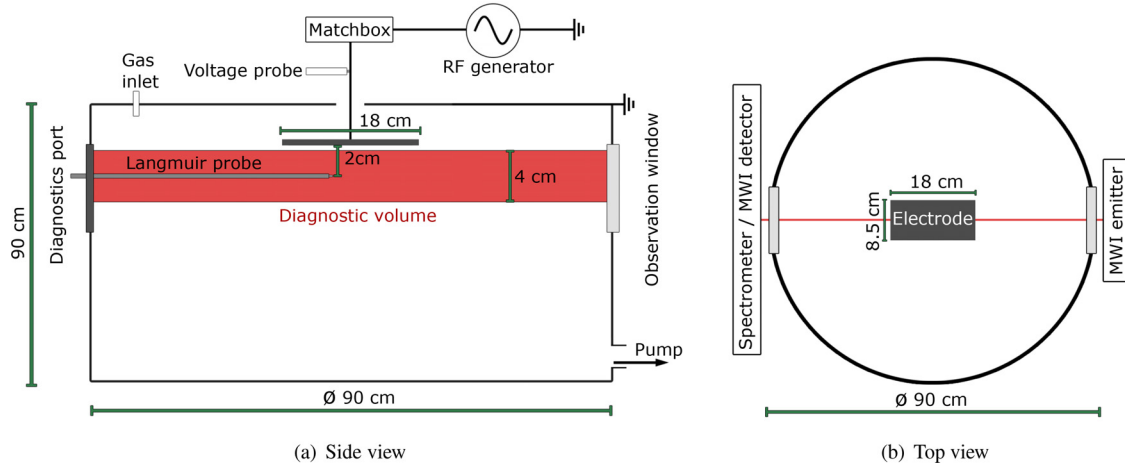


FIG. 1. (a) Side and (b) top view schematic of the experimental setup. The cut in (b) is at the vertical position marked as diagnostic volume in (a). The relevant dimensions together with the arrangement of the various diagnostics are also shown.

pressure gauge (CCR 365, Pfeiffer Vacuum). Flow rates in the range of 4–40 sccm are used.

The capacitive discharge is ignited between a powered electrode at the top of the vacuum chamber and the grounded metal walls, producing a geometrically asymmetric discharge (symmetry parameter $\varepsilon < 0.4$). The powered electrode is a tungsten plate with a length of 18 cm and a width of 8.5 cm. Water circulating behind the plate provides a stable operating temperature. A stainless steel grounded plate around the powered electrode acts as a guard ring to prevent discharge ignition on the side of the powered electrode. This yields a homogeneous sputtering of the flat side of the tungsten plate. The guard ring is spaced 0.2 cm apart from the electrode to avoid a short circuit, which would occur if it comes into contact with the electrode, for example, due to thermal expansion. This distance further ensures no plasma penetration between the electrode and the guard ring while keeping the displacement current to the guard ring at a reasonable level.

The powered electrode is biased by a radio-frequency (RF) signal at $\omega_{\text{RF}}/2\pi = 60$ MHz supplied by a RF-power generator (cito Plus, Comet). An impedance matching network (AGS 6020a, Comet) minimizes the reflected power. For all investigated conditions, it typically does not exceed 1 W. The matching network is placed on top of the vacuum vessel to be as close as possible to the powered electrode.

B. Diagnostics

The voltage at the tungsten electrode is measured by a high-voltage probe (P6015A, Tektronix, bandwidth 75 MHz) linked to an oscilloscope (WaveSurfer 424, LeCroy, bandwidth 200 MHz). The probe directly samples the potential on the wire connected to the powered electrode consisting of the externally applied voltage waveform $V_{\text{RF}}(t)$ shifted by a constant self-bias η [see Eq. (15)].

A microwave interferometer (Miwitron, MWI2650) operating at a frequency $\omega_{\text{MW}}/2\pi = 26.5$ GHz is used to determine the line-integrated electron density in a region below the powered electrode. The region [marked as diagnostic volume in Fig. 1(a)] has a diameter of about 4 cm and is located 2 cm below the tungsten electrode. The microwave interferometer (MWI) measures the phase shift between

the microwave beam sent through the plasma and the signal propagating through vacuum. The phase shift is related to the line-averaged plasma density \bar{n}_e ,²⁸

$$\Delta\varphi \approx \frac{e^2}{2\varepsilon_0 m_e c \omega_{\text{MW}}} \int_{-R}^R n(x) dx = \frac{e^2}{2\varepsilon_0 m_e c \omega_{\text{MW}}} 2R \bar{n}_e, \quad (1)$$

where ε_0 denotes the vacuum permittivity, e is the elementary charge, c is the speed of light, and m_e is the electron mass.

The value of the plasma density on the discharge axis [$n_0 = n(r = 0 \text{ cm})$] is determined from MWI measurements by measuring the density profile using a Langmuir probe. The probe has a tungsten tip with a diameter of 0.05 cm and a length of 1 cm. The probe is movable in the radial direction in a plane situated 2 cm below the powered electrode corresponding to the middle of the diagnostic volume [Fig. 1(a)]. Due to the high value of the RF frequency, it is difficult to achieve good suppression of the RF disturbance on the probe characteristics. Instead only the current at a large negative voltage (-32 V) is measured. This part of the probe characteristics (ion saturation current) is largely insensitive to the RF oscillations of the plasma potential, eliminating the need for RF compensation circuitry. Furthermore, no attempt is made to extract the electron density from the measured ion saturation current, since the relation depends on the operation regime of the probe.^{29,30} Instead, the spatial profile of the saturation current $I_{i,\text{sat}}(r)$ is assumed to coincide with the profile of the density $n(r)$. Indeed, the ion saturation current, collected by the probe, is $I_{i,\text{sat}} \propto S_p n u_B$. The Bohm velocity depends on the square root of the electron temperature T_e : $u_B \propto \sqrt{T_e}$. However, the collection area for a cylindrical probe in the orbital motion limited (OML) theory is inversely proportional to the square root of T_e : $S_p \propto \sqrt{eU/k_B T_e}$, where k_B is the Boltzmann constant and U the probe bias (relative to the plasma).^{31,32} Then, the measured current is largely insensitive to the variations in the electron temperature and the main source of error is due to the accuracy of the current measurements. The relative uncertainty related to that does not exceed 1%. The spatial profile of the saturation current in a combination with the line-

averaged value from the MWI measurements is then used to obtain the values of the plasma density along the radius of the chamber (Sec. III A).

A four-channel spectrometer (AvaSpec-2048FT-4-DT, Avantes) combined with an optical fiber provides the emission spectra of the discharge for optical emission spectroscopy (OES). The specifications of the spectrometer are summarized in Table I. The spectrometer is relatively calibrated using an Ulbricht sphere (BN-0102, Gigahertz-Optik). The fiber is connected to a collimator that ensures the collection of light emitted solely parallel to the biased electrode. The collimator can be affixed to predefined positions in front of the window (vertical distances to the electrode: 0.5, 1.5, 2.5, 4.5, and 6.5 cm). Note that only the first three of these regions cover the diagnostic volume. Backlight illumination through the optical setup yielded a spot size of about 1 cm in the region below the electrode.

III. PLASMA PARAMETERS

For the removal of coatings from metallic mirrors using a high-frequency CCP, the sputter rates and the flux of sputtered atoms of the surface material are the crucial quantities that depend on the plasma parameters. The flux density of the sputtered tungsten atoms, Γ_W , leaving the surface assuming an infinitely large target (Fig. 1) is given by

$$\Gamma_W = \Gamma_{Ar^+}(n_0, T_e) Y(E_{kin, Ar^+}). \quad (2)$$

The sputter yield, Y , is determined by the kinetic energy of the impinging argon ions, E_{kin, Ar^+} . The flux density of these ions, Γ_{Ar^+} , depends on the plasma density in front of the electrode, n_0 , and the electron temperature, T_e . Sections III A to III C 2 present the methods used to extract n_0 , T_e , and E_{kin, Ar^+} from the experimental data and show their variations with the discharge conditions (power and pressure). Table II provides as a reference an overview of the obtained plasma parameters.

A. Electron density

The first important plasma parameter is the electron density. Naturally, at the low working pressures considered here, the density is not homogeneous throughout the discharge due to the strong influence of diffusion. This aspect needs to be considered when determining the density.

1. Density profile

The electron density is obtained by combining microwave interferometer measurements with Langmuir probe measurements of the ion saturation current. At low pressures, the spatial profile of the saturation current, i.e., of the plasma density, is governed by the ionization

TABLE I. Specifications of the four-channel USB spectrometer.

Channel	Dispersion (nm/px)	λ_{min} (nm)	λ_{max} (nm)
1	0.02	594	642
2	0.05	373	471
3	0.04	491	564
4	0.25	591	1105

TABLE II. Peak electron density n_0 , effective electron temperatures close to the sheath edge ($z = 0.5$ cm) from the collisional-radiative model $T_{e, CRM}$ and from the fit of the diffusion profile $T_{e, FDP}$, average accelerating potential \bar{V}_s and maximal sheath thickness s_m at different pressures and an RF power of 100 W.

Pressure (Pa)	n_0 (10^{16} m^{-3})	$T_{e, FDP}$ (eV)	$T_{e, CRM}$ (eV)	$-\bar{V}_s$ (V)	s_m (cm)
0.5	1.1	2.3	2.9	184	0.36
1	2.0	2.1	2.5	177	0.26
3	4.4	1.6	2.3	157	0.17
10	5.9	1.3	1.6	114	0.12

of neutral particles and the diffusion of electrons and ions. Consequently, the gas density and the electron temperature determine the shape of the electron density profile. Both of these quantities are essentially independent from the coupled power but change with the gas pressure. The dependence of the electron temperature on the pressure (p) is³³

$$T_e \propto 1/\log(p). \quad (3)$$

Therefore, the electron density profiles were measured at a single power level of 30 W and various pressures in the range 0.5–10 Pa. The results are shown in Fig. 2.

Under all conditions, the profiles exhibit two relatively distinct regions. In these, the processes driving the ionization differ substantially. Near the discharge axis, i.e., in the region below the powered electrode, the beam of energetic electrons produced by the sheath expansion contributes significantly to the ionization process. Outside of this region, the ionization, when present at all, is driven by the bulk plasma electrons.

To describe and to better understand this behavior, a simple model for the profile of the density $n(r)$ is developed. It is based on a solution of the one-dimensional steady-state diffusion equation. In cylindrical coordinates with azimuthal symmetry, it is given by

$$\frac{d^2 n}{dr^2} + \frac{1}{r} \frac{dn}{dr} + \frac{\nu_{iz}}{D} n = 0, \quad (4)$$

where D is the ambipolar diffusion constant.³³ Note that in this model, the ionization frequency, ν_{iz} , is an effective one that accounts also for the diffusion in the axial direction. Therefore, it is expected that its value will be lower than the one that can be estimated from the distribution function of the electrons, i.e., from the electron temperature.⁷⁷

The difference in the mechanisms for ionization is captured in the model through an approximation of the term $A = \nu_{iz}/D$ by a step profile,

$$A = \begin{cases} A_1, & 0 \leq r \leq r_0 \\ A_2, & r_0 \leq r \leq R. \end{cases} \quad (5)$$

Here, r_0 is the radial position that separates the two regions. Its value is expected to be close to the position of the edge of the electrode ($r = 9$ cm). At this position, the density profile has to be continuous. Note, however, that due to the jump in the source term A , the derivative of the density cannot be continuous at $r = r_0$. The other boundary conditions are for a finite plasma density in the center equal to $n(0) = n_0$ and a vanishing density at the walls $n(R) = 0$. The former is an

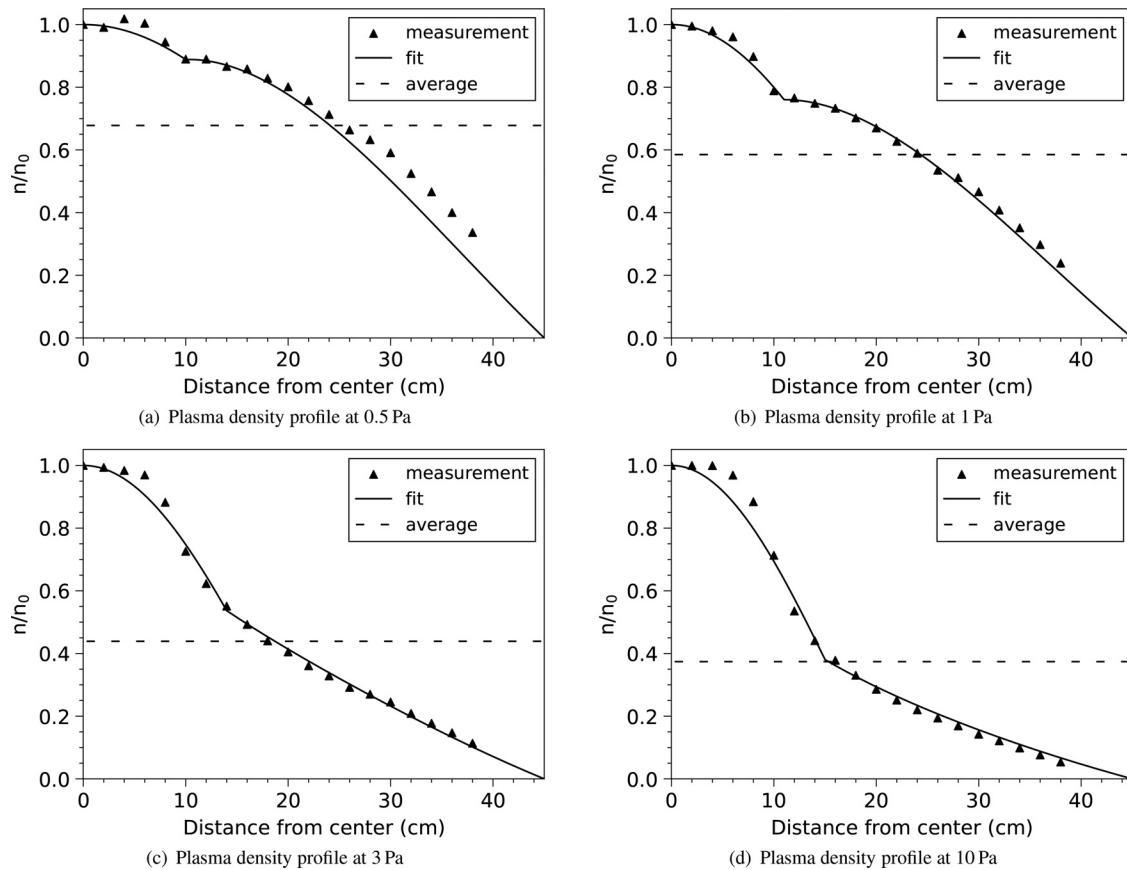


FIG. 2. Measured profiles of the plasma density at a power of 30 W and a pressure of (a) 0.5 Pa, (b) 1 Pa, (c) 3 Pa, and (d) 10 Pa. The fit of Eq. (6) (continuous curve) is also shown together with the line-averaged plasma density \bar{n}_e/n_0 (dashed line).

arbitrary scaling constant that cannot be determined from the diffusion equation, but is given by the energy balance of the electrons. The latter condition is motivated by the fact that the radius of the vacuum chamber, R , is much larger than the mean free path of the ions, causing the density near the walls to drop to much lower values than in the center.

With these boundary conditions, the solution to Eq. (4) is given by

$$\frac{n(r)}{n_0} = \begin{cases} J_0(\sqrt{A_1}r), & 0 \leq r \leq r_0 \\ \gamma J_0(\sqrt{A_2}r) + \delta Y_0(\sqrt{A_2}r), & r_0 \leq r \leq R. \end{cases} \quad (6)$$

Here, J_0 and Y_0 are the zero-order Bessel functions of the first and second kind, respectively. The values for the constants γ and δ follow from the boundary conditions:

$$\gamma = \frac{J_0(\sqrt{A_1}r_0)Y_0(\sqrt{A_2}R) - Y_0(\sqrt{A_1}r_0)J_0(\sqrt{A_2}R)}{J_0(\sqrt{A_2}r_0)Y_0(\sqrt{A_2}R) - Y_0(\sqrt{A_2}r_0)J_0(\sqrt{A_2}R)}, \quad (7)$$

$$\delta = \frac{-J_0(\sqrt{A_1}r_0)J_0(\sqrt{A_2}R)}{J_0(\sqrt{A_2}r_0)Y_0(\sqrt{A_2}R) - Y_0(\sqrt{A_2}r_0)J_0(\sqrt{A_2}R)}. \quad (8)$$

In the classical textbook case $A_1 = A_2 = A_0$, the above solution yields the well-known Bessel profile,

$$\frac{n(r)}{n_0} = J_0(\sqrt{A_0}r), \quad (9)$$

together with the Schottky condition $\sqrt{A_0} = 2.405/R$. This condition leads to relation (3).

The experimental density profiles are compared to the analytical prediction of Eq. (6). For the comparison, the constants A_1 , A_2 , and r_0 are varied. The fits are shown in Fig. 2, and the numerical values for the fitted parameters are provided in Table III.

At all pressures, the essential features of the experimental profiles are well captured by the analytical expression [Eq. (6)]. This highlights

TABLE III. Values of the fitting parameters A_1 , A_2 , and r_0 in Eq. (6). The ratio of the resulting line-averaged density \bar{n}_e to the center plasma density n_0 is also given.

Pressure (Pa)	A_1 (m ⁻²)	A_2 (m ⁻²)	r_0 (cm)	\bar{n}_e/n_0
0.5	46.0	34.1	10	0.678
1	84.5	34.9	11	0.585
3	108.0	16.2	14	0.439
10	133.1	9.0	15	0.374

the importance of considering the inhomogeneities in the ionization for the studied discharge configuration. The smallest deviation from the usual Bessel profile, described by Eq. (9), is observed at the lowest investigated pressure (0.5 Pa). Nonetheless, the quantity A is in both regions substantially higher than the expected value of $(2.405/R)^2 \approx 28.6 \text{ m}^{-2}$. This indicates significant inhomogeneities in the ionization frequency, which is not unexpected since the fast beam-like electrons generated at the oscillating sheath edge are a vital contribution to the ionization frequency. The two values become increasingly distinct as the pressure rises, and considerable deviation from a Bessel profile is observed. In the inner region, the value of A_1 increases, whereas A_2 decreases (Table III). The former causes a larger plasma inhomogeneity in the central region due to a faster drop of the plasma density with the radius, while the latter causes a change in the sign of the curvature of the density profile. This is explained by a decrease in the ionization frequency in the outer region, which reduces the effect of the ionization term in Eq. (4). Consequently, the density profile begins to be dominated by the expansion of the plasma rather than the ionization, leading to a change in its curvature.

Likewise, the transition point r_0 between the inner and outer region shifts outward as the pressure rises. The observed shift results from an increased collisionality of the electrons leading to the central region of stronger ionization becoming more diffuse and expanding outward.

Note that the density within the extent of the electrode ($r \leq 9 \text{ cm}$) remains fairly homogeneous. The variation is for all conditions within 15% from the value on the axis n_0 . This effect together with possible variations of the sheath voltage due to edge effects would determine the homogeneity of the treatment of the mirror surface. Note that depending on the severity and the type of depositions, a homogeneous treatment might not necessarily be the optimal solution. However, the investigations and the optimization of the sputtering homogeneity is beyond the scope of the present studies.

Given these density profiles, the ratios of averaged (\bar{n}_e) to peak (n_0) electron density are obtained. Linear extrapolations of the profiles close the chamber walls account for the missing experimental data points. The values obtained for the different pressures are listed in Table III and are also represented in Fig. 2. This ratio is needed to convert the line-averaged density \bar{n}_e , measured by the MWI, into a density in the center n_0 . Knowing the value of n_0 and the density profile yields the plasma density at any other position.

Figure 3 shows the peak plasma densities derived from the experimental data for different RF powers and gas pressures. As expected, the density at a given power level increases with the pressure. The rise with the power at a fixed gas pressure is non-linear and follows a nearly square root dependence,

$$n_0 = \alpha \sqrt{P}, \quad (10)$$

which is in good agreement with the general theory of capacitive discharges assuming a collisionless sheath.³³

2. Argon collisional-radiative model

For comparison, the electron density is also obtained from the emission spectra of the discharge. Unlike the probe measurements, this is a non-invasive method. However, its disadvantage is that the collected emission is a line-averaged quantity. Typically, the

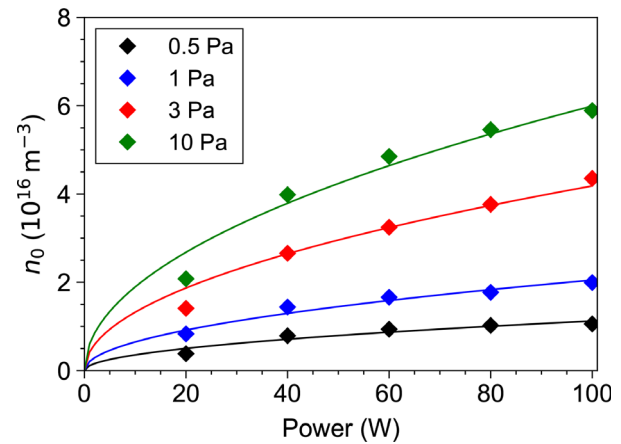


FIG. 3. Plasma density n_0 on the axis, i.e., in front of the electrode obtained from MWI and probe measurements.

assumption for spatially homogeneous plasma parameters is implicitly invoked for the interpretation of the spectra.^{34–37}

In this work, the argon collisional-radiative model (CRM) developed for conditions present in a cylindrically symmetric CCP by Siepa *et al.*^{38,39} is used to obtain the electron density and temperature. The population densities of the 14 energetically lowest states of the neutral argon atom are modeled by accounting for electron impact excitation, radiation trapping, metastable pooling, and diffusion to the walls. The radiation trapping is considered for a cylindrical geometry⁴⁰ with a radius of $R = 45 \text{ cm}$. The model then provides the emission intensities expected for a given value of the electron temperature and density $I_{\text{CRM}}(\bar{n}_e, T_e)$. By comparing the calculated to the measured intensities, the values of the plasma parameters can be extracted.

For such a procedure, the intensities have to be measured by a radiometrically absolutely calibrated detector. Typically the absolute calibration is achieved by carefully positioning a light source with known radiance into the vacuum chamber. Comparing the measured to the expected intensity yields the calibration factors for the investigated transition.^{41–43} However, this is a time-consuming procedure and more commonly the method of the line-ratios is applied.^{44,45} In this approach, instead of adjusting the individual intensities, the collisional-radiative model tries to match the ratios of two or more emission lines obtained in the experiment. Using spectrally close lines avoids large variations in the sensitivity of the detection system. Then, in the ratio of the two intensities, the unknown calibration factors cancel out. Siepa *et al.*³⁸ have recommended two pairs of line intensities as suitable for use with the line ratio method: the ratio $I_{706.7 \text{ nm}}/I_{750.4 \text{ nm}}$ as being sensitive to the electron density and the ratio $I_{763.5 \text{ nm}}/I_{738.4 \text{ nm}}$ as being sensitive to the electron temperature.³⁸ Figure 4 shows a typical argon spectrum with these lines marked in it. Note that the resolution of the spectrometer allows the line at 750.4 nm to be well separated from its neighboring line at 751.47 nm, allowing its use for the diagnostics.

Despite its wide use, this approach also has some disadvantages. In particular ranges of the plasma parameters, the emission intensities of most lines have a nearly linear dependence on the electron density.

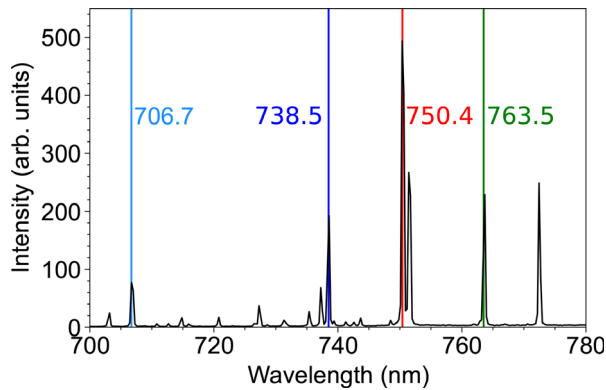


FIG. 4. Example spectrum of an argon discharge at 3 Pa, 100 W and a vertical distance to the electrode of 0.5 cm. The lines used for the line-ratio method are marked by colored vertical bars.

For example, in tenuous plasmas, the direct excitation from the ground state is the dominant population mechanism of the excited states (corona limit), while in dense plasmas, the population of the metastable states is saturated and ceases to depend on the electron density.⁴⁶ Then, the ratio of any two emission lines becomes relatively insensitive to the electron density. The result is that the value for this parameter becomes less reliable when inferred from collisional-radiative models that use the line-ratio method.

To circumvent this problem, while avoiding the difficulties of the standard procedure for absolute calibration, in this work, an alternative approach is employed. A set of discharge parameters is chosen, where the intensities of the spectral lines keep their non-linear dependence on the electron density. For our conditions, this was the case for a pressure of 3 Pa and a power level of 60 W and above. Then, the line-ratio method is applied to extract the plasma parameters. Finally, these parameters are used to calculate the emission intensities. Through comparison with the experimentally measured ones, calibration factors F are determined for each line:

$$I_{\text{CRM}} = F I_{\text{OES}}. \quad (11)$$

These factors are then used for all other conditions to extract the plasma parameters from the individual emission intensities (763.5 nm, 738.4 nm). In this way, a significant improvement between the electron densities obtained by this method and by the MWI is achieved (Fig. 5). The agreement between the two diagnostic techniques is very good, and the same trends in the behavior of the electron density with the power and the pressure are again observed. The improvement in the agreement can also be quantified by the relative mean deviation from the MWI density values:

$$\chi = \frac{1}{N} \sum_{i=1}^N \left| 1 - \frac{\bar{n}_{e,i,\text{rel/abs}}}{\bar{n}_{e,i,\text{MWI}}} \right|. \quad (12)$$

Here, the summation covers the different power levels for a given pressure. The result is presented in Fig. 6. The unreliability for determining the electron density from the ratio of two line intensities at the lower pressures (0.5 and 1 Pa) become apparent from the large discrepancies with the MWI data (up to 90%).

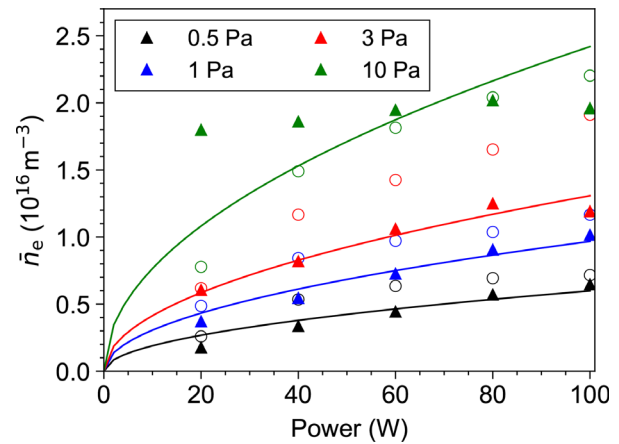


FIG. 5. Line-averaged electron density at a distance of 0.5 cm from the electrode determined by the CRM (full triangles) using the absolute calibration procedure. The curves are fits of Eq. (10). The line-averaged data from the MWI are also shown for comparison (open circles).

B. Electron temperature

The approach developed in Sec. III A 2 is also beneficial for determining the electron temperature from the respective neutral argon lines (763.5 nm, 738.4 nm). The electron temperature is the second important plasma parameter for the flux of the sputtered atoms [Eq. (2)]. First estimations for an effective value of this parameter are obtained from the fits of the density profiles (Sec. III A 1) and compared to the values obtained from the emission spectra via the CRM (Sec. III A 2).

1. Fit of the diffusion profile

The shape of the density profile depends on the source (ionization), whose properties are governed by the electron temperature. The fitting parameters A_1 and A_2 of the model developed in Sec. III A 1 are related to the ionization frequencies in the inner and the outer plasma

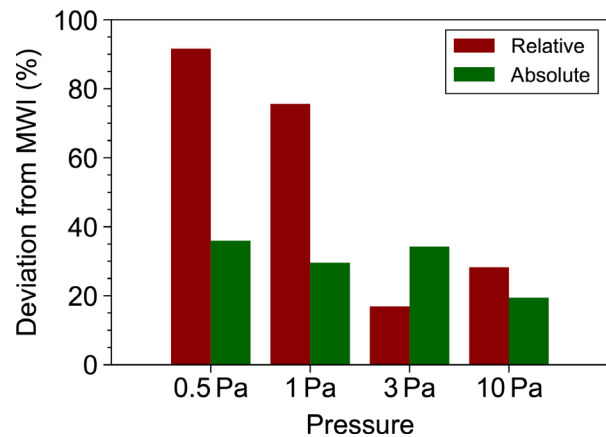


FIG. 6. Relative deviation between the CRM and MWI data [Eq. (12)] averaged over the various power conditions. The cases when using line ratios (relative) and individual intensities (absolute) are compared.

regions, respectively. This allows estimating the electron temperature from the values of the fitting parameters.

When the electron temperature is much higher than the ion temperature T_i ($T_e \gg T_i$), the ambipolar diffusion coefficient is given by $D \approx \mu_i k_B T_e / e$, with μ_i the mobility of the ions.³³ The ionization frequency is given by $\nu_{iz} = n_{\text{gas}} K_{iz}$, where n_{gas} is the neutral gas density and K_{iz} the ionization rate coefficient. Then the parameters A_i ($i = 1, 2$) are related to the electron temperature by

$$A_i(T_e) = \frac{\nu_{iz}}{D} = \frac{en_{\text{gas}}K_{iz}(T_e)}{\mu_i k_B T_e}. \quad (13)$$

Using the mobility for argon ions in their own gas given by McDaniel and Mason⁴⁷ and calculated ionization rate coefficient for a Maxwellian distribution of the electrons^{48,49} provides the basis of the electron temperature estimation. For that, the non-linear relation between T_e and A_i is inverted numerically.

The neutral gas density is obtained from the ideal gas law, assuming that the gas is at room temperature (300 K). The resulting values for T_e in the inner and the outer region are shown in Fig. 7. Both temperatures show a nearly logarithmic dependence on the pressure [Eq. (3)], as would be expected from the Schottky condition $A_i(T_e) = \text{const.}$ Here, due to the presence of two distinct regions, this condition is not exactly met. Nevertheless, the general trends remain the same.

A higher value of A_1 relative to A_2 correlates with a higher electron temperature in the vicinity of the electrode compared to the outer plasma regions. This is in accordance with the presence in the inner region of energetic electrons, created by the sheath expansion. With an increase in pressure, the electron temperature in both the inner and the outer region decreases in conformity with the general trends of low-pressure discharges. However, the decrease in the outer region is more pronounced than the one in the inner region as evidenced by the increase in the relative difference $(T_2/T_1 - 1)$ (Fig. 7). The reason is the reduced energy and particle transport in the radial direction due to the larger collisionality of the electrons when the pressure is higher. This prevents the temperatures in the two regions from equilibrating. Without a compensating energy source, the electron temperature decreases faster with the radial distance.

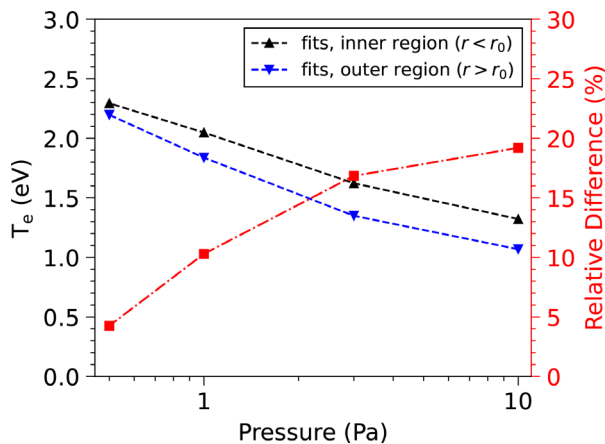


FIG. 7. Electron temperature obtained from the fitting coefficients for the plasma density profiles (Table III) using Eq. (13). Applied power 30 W.

2. Argon collisional-radiative model

The electron temperature is obtained also via the CRM (Sec. III A 2) from the spectra taken at different vertical distances from the electrode. The reliability of the values for this parameter is much higher than for the electron density due to the strong dependence of the measured emission spectra on the electron temperature. The values obtained from the spectra at 0.5 cm from the electrode are shown in Fig. 8. These are the values used later on for estimating the ion flux to the electrode. As expected, the electron temperature does not depend on the applied power. Close to the electrode [Fig. 8(a)], the same nearly logarithmic dependence on the pressure [Eq. (3)] is observed. The comparison with the values obtained from the density profiles also shows good agreement. Here, the values for the inner region ($r < r_0$) are taken since the temperature there is higher. Consequently, most of the plasma emission originates from this region. For this reason, the value of the electron temperature from the CRM would be representative for the inner bright plasma volume.

A comparison of the temperature obtained for different distances from the electrode [Fig. 8(b)] shows that it decreases with the distance. The decrease becomes even more pronounced when the pressure is higher [Fig. 8(c)]. This inhomogeneity in the vertical direction correlates well with the one in the radial direction, obtained from the profiles of the plasma density. The reason is the same—the increasing electron collisionality reduces the transport of energy. Then, at higher pressures, the energetic electrons remain close to the sheath region where the energy from the stochastic heating by the oscillating sheath edge is deposited.^{50–52}

C. Ion impact energy

The sputtering of the tungsten electrode is driven by the argon ions, which impinge onto its surface. The corresponding sputter yield strongly depends on the impact energy of the projectiles. Generally, the ions are not mono-energetic but distributed over an energy interval. A typical ion energy distribution function, assuming a collisionless RF sheath, is bimodal.⁵³ However, due to the high value of the RF frequency of 60 MHz and the relatively large mass of the argon ions, the energy difference between the two peaks becomes small. In essence, all ions transiting through the sheath are subject to the same average accelerating potential yielding a single-peak ion energy distribution function. In this case, the ion energy is practically monoenergetic and can be estimated from voltage waveform measurements at the driven electrode.

1. Analytical model of the RF-sheath

The first step is to estimate the accelerating potential using the analytical model for the RF sheath by U. Czarnetzki.⁵⁴ For a driven electrode, whose surface area is much smaller than that of the grounded electrode, the voltage drop V_s over the sheath in front of it can be expressed by

$$V_s(t) \approx (\eta - V_{\text{RF}}) \sin^{2(1+\epsilon/a)}\left(\frac{\omega_{\text{RF}} t}{2}\right). \quad (14)$$

Here, V_{RF} denotes the amplitude of the externally applied sinusoidal voltage waveform and $\eta < 0$ corresponds to the self-bias, which arises due to the geometric asymmetry of the discharge. The cubic correction

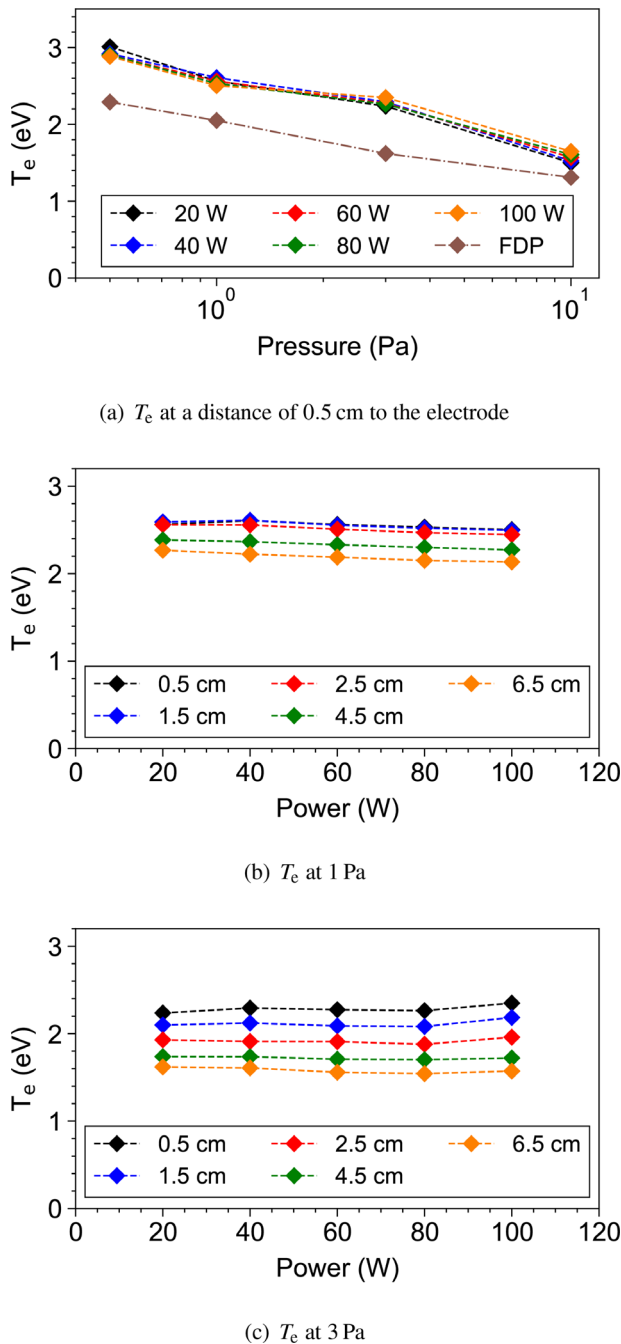


FIG. 8. Line-averaged effective electron temperature obtained from the CRM. (a) Pressure variation at a distance of 0.5 cm from the electrode. For comparison, the values for the inner region ($r < r_0$) from the fit of the diffusion profile (FDP) are also given. (b) Power variation at 1 Pa and various distances from the electrode. (c) The same as in (b) for a pressure of 3 Pa. The curves are only guides for the eye.

parameter a in the collisionless case has the value of $a = 1.56$.⁵⁴ The value of the asymmetry parameter ε is determined from η and V_{RF} according to Ref. 54. The voltage waveform at the position of the driven electrode (V_{DE}), i.e., the voltage drop over the entire discharge, is

$$V_{DE}(t) = \eta + V_{RF} \cos(\omega_{RF} t). \quad (15)$$

In this work, the values of η and V_{RF} are obtained through fitting of this relation to the data from the voltage probe. The time-averaged sheath voltage (\bar{V}_s) is obtained by averaging Eq. (14),

$$\bar{V}_s = (\eta - V_{RF}) \frac{1}{2\pi} \int_0^{2\pi} \sin^{2(1+\varepsilon/a)}(\phi/2) d\phi < 0. \quad (16)$$

Then, the energy of the ions bombarding the electrode is given by

$$E_{kin,Ar^+} = E_B - e\bar{V}_s, \quad (17)$$

where the additional energy $E_B = k_B T_e / 2$ is related to the finite Bohm velocity $u_B = \sqrt{k_B T_e / m_{Ar^+}}$ of the ions at the sheath edge. Figure 9 presents the corresponding impact energies of the argon ions, assuming a collisionless propagation through the sheath. Note that the sputtering threshold energy of tungsten by the argon-ion bombardment²⁵ of $E_{th} = 27$ eV is surpassed for all experimental conditions investigated in this work.

2. Collisions in the sheath

The approximation for monoenergetic ions with an energy given by Eq. (17) is valid only when the sheath is collisionless. This is the case when the ion mean free path,

$$\lambda_{mfp} = \frac{1}{n_{gas} \sigma(E)}, \quad (18)$$

which is related to the energy-dependent momentum transfer cross section $\sigma(E)$, is substantially larger than the maximum sheath extension s_m ($\lambda_{mfp} \gg s_m$). More precisely, the fraction of ions that traverse the sheath without a single collision with the background gas is given by

$$f_{no.col.} = \exp \left(-n_{gas} \int_0^{s_m} \sigma(E(x)) dx \right). \quad (19)$$

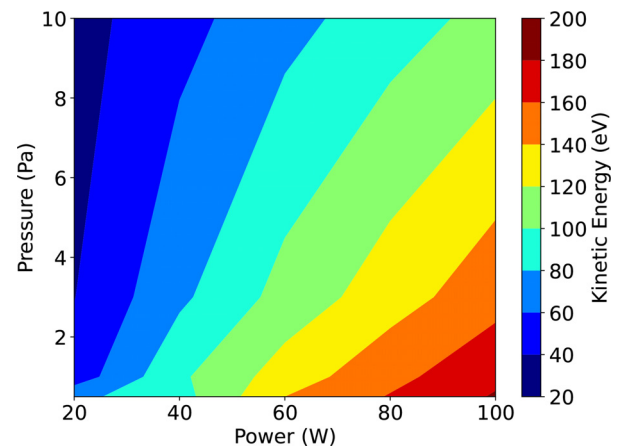


FIG. 9. Impact energy of singly ionized argon atoms bombarding the electrode.

To estimate this fraction, the cross section for momentum transfer collisions of argon ions with argon atoms is taken from Phelps.⁵⁵ The gas density n_{gas} is evaluated from the ideal gas law for a gas temperature of 300 K. The maximum sheath thickness s_m is estimated by combining the collisionless Child-Langmuir law for RF sheaths,⁵⁴

$$\Gamma_{\text{Ar}^+} \approx 1.2\epsilon_0 \sqrt{\frac{2}{em_{\text{Ar}^+}}} \frac{|\bar{V}_s|^{3/2}}{s_m^2}, \quad (20)$$

with the ion flux at the sheath edge

$$\Gamma_{\text{Ar}^+} = n_i u_B. \quad (21)$$

This gives for the maximum sheath thickness

$$s_m \approx 1.3\lambda_D \left(\frac{e|\bar{V}_s|}{k_B T_e} \right)^{3/4}, \quad (22)$$

where λ_D is the Debye length at the sheath edge.

For a matrix sheath, the energy E of collisionless ions at any point x within the sheath is given by

$$E(x) = E_B - e\bar{V}_s \left(\frac{x}{s_m} \right)^2. \quad (23)$$

This allows numerical integration in Eq. (19) to be performed. Figure 10 shows the results of these estimations. It is seen that for pressures up to 3 Pa, the vast majority of argon ions reach the electrode without collisions. This justifies the assumption for monoenergetic ions. For the results at 10 Pa, this is no longer the case and Eq. (17) likely overestimates the ion impact energy.

IV. SPUTTER RATES OF TUNGSTEN

With the plasma parameters available, the flux of sputtered tungsten atoms resulting from bombardment by normally incident argon ions can be obtained via Eq. (2) to

$$\Gamma_W = n_0 u_B(T_e) Y(E_{\text{kin,Ar}^+}), \quad (24)$$

where the individual components are directly linked to the measured plasma parameters. The sputter yield Y can be approximated using the empirical formula by Eckstein and Preuss.^{24–26} An alternative empirical formula was developed by Yamamura and Tawara.⁵⁶ However, it

does not fit that well the experimental data near the threshold energy.⁵⁷ From the flux of the sputtered atoms also the sputter rate, i.e., the change in the electrode thickness per unit time, can be calculated by

$$\Theta = \Gamma_W \frac{m_W}{\rho}. \quad (25)$$

This quantity is central for the speed with which tungsten coatings can be removed. In Eq. (25), m_W is the mass of the tungsten atoms and $\rho = 19250 \text{ kg/m}^3$ is the mass density of tungsten at room temperature.⁵⁸

The resulting sputter rates at the different discharge conditions are given in Table IV. The difference in the values of the effective electron temperature is not significant for the final results, since the relative deviation of the sputter rates obtained with the two effective temperatures (CRM and fit of the diffusion profile—FDP) does not exceed 10%.

The sputter rates obtained from Eq. (25) generally increase with the discharge power since the plasma density also increases, which causes a rise of both the argon-ion flux and the self-bias at the electrode. The latter is the major contributor to the increase in the sputter rate since it depends strongly on the kinetic energy of the argon ions. This energy must be low enough to avoid damaging the mirror, especially when it is made of a lower- Z material.

Figure 11 shows the sputter rate for different pressures and impact energies of the argon ions. It becomes evident that the sputter rate depends primarily on the energy of the bombarding ions through the sputter yield Y . The dependence on the pressure p , most prominent in the range of lower pressures, is due to the different variation of n_0 and E_{kin} with p .

For a given power, the sputter rates peak around 3 Pa (Table IV). The maximal value of $\Theta = 2.6 \text{ Å/s}$ appears at a pressure of 3 Pa and an applied RF power of 100 W. Generally, the sputter rates obtained for the pressure range of 1–10 Pa correspond to about a monolayer per second. The removal rate can be additionally controlled by adjusting the discharge power. The sputter rates correspond well also with the value of 0.83 Å/s obtained at PSI-2 in an Ar–H plasma for argon ions with an energy of 180 eV.⁸ Despite the plasma of PSI-2 being much denser than the present discharge, the sputter rates obtained there are lower than the ones in the present study due to the presence of hydrogen. The large difference in the mass of the hydrogen ions and of the tungsten atoms results in a negligible sputter yield. These results suggest that the addition of hydrogen could be used as another means for adjusting the sputter rates. A cleaning regime can be recommended, where the gas composition consists of about 80% hydrogen

TABLE IV. Estimated sputter rates of tungsten atoms by argon ions for the conditions investigated in this work (plasma parameters listed in Table II). The sputter rates are in Å/s.

	20 W	40 W	60 W	80 W	100 W
0.5 Pa	0.03	0.13	0.5	0.8	1.0
1 Pa	0.006	0.3	0.8	1.2	1.7
3 Pa	0.002	0.18	0.8	1.6	2.6
10 Pa	0.0003	0.04	0.24	0.6	1.2

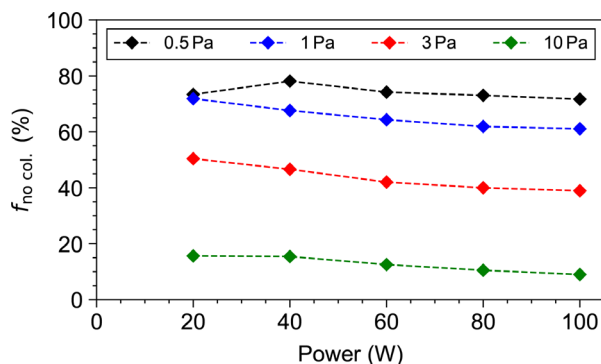


FIG. 10. Percentage of ions that traverse the sheath without collisions with the background gas. Its density is calculated for a gas temperature of 300 K.

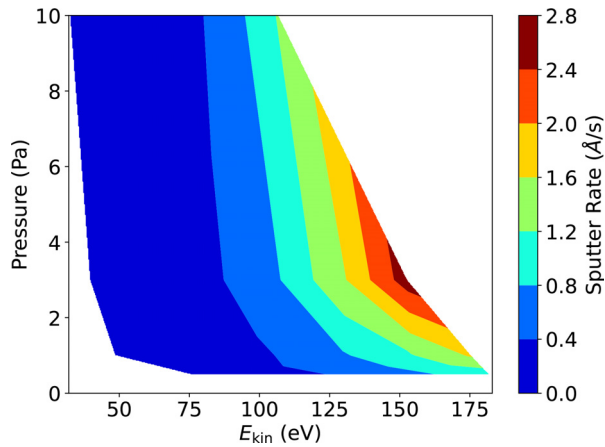


FIG. 11. Contour plot of the sputter rates of a tungsten surface bombarded by argon ions. The white area represents the absence of experimental data at these conditions.

and an admixture of 20% argon. The latter could be supplied in the torus filling or through local injection at the position of the mirror. This operation scenario might be enough to (i) adjust the sputter rate, (ii) sputter the other impurities beside Be (Fe from the diagnostic plug is expected to be the main contributor⁶), and (iii) make use of Doppler shifted reflectance measurement (DSRM)^{59–61} as an end-of-cleaning indicator as explained in the outlook (Sec. V) below.

In Secs. IV A–IV C 2, the emission of sputtered tungsten atoms is used directly as an indicator for evaluating the validity of the sputter rates determined in Sec. IV. This evaluation is performed in two ways. Firstly, the sputter rates and plasma parameters provide the input into a simple model of tungsten line emission, and the behavior of the intensities with the power and the pressure is compared to OES measurements. Secondly, the relative sputter yield is derived by using the measured values of the plasma parameters (electron density and temperature, sheath voltage) and the intensity of the tungsten lines. The result is compared to the predictions of the empirical formula by Eckstein and Preuss,^{24–26} essentially providing an experimental benchmark of that formula.

A. Tungsten line intensity

The relation of the intensity of the tungsten emission to the plasma parameters is given by the definition of an intensity. For an electric dipole transition from an initial atomic state i to an energetically lower state j , it is given by⁶²

$$I_{i \rightarrow j} = \frac{hc}{4\pi\lambda} A_{ij} 2R n_{W,i}, \quad (26)$$

where h is the Planck constant, λ is the center wavelength of the transition, $2R = 90$ cm is the length of the emitting plasma, and A_{ij} is the Einstein coefficient for spontaneous emission. The density $n_{W,i}$ of the atoms in the state i is estimated in the Corona limit as

$$n_{W,i} = \frac{n_0 n_{W,g.s.} K_{exc}(T_e)}{\sum_j A_{ij}}, \quad (27)$$

where $K_{exc,i}(T_e)$ denotes the rate coefficient for electron impact excitation from the ground state with a density $n_{W,g.s.}$. The rate coefficient for low electron temperatures can be expressed in terms of the Arrhenius equation as^{63–65}

$$K_{exc,i}(T_e) = q_0 \exp \left\{ -\frac{E_i}{k_B T_e} \right\}, \quad (28)$$

where E_i is the threshold energy for the process and the coefficient q_0 has only a weak (at most polynomial) dependence on the electron temperature. This dependence is neglected in the following treatment. Then, the intensity of the emission from the sputtered tungsten atoms is given by

$$I_{i \rightarrow j} = \bar{C} n_0 n_{W,g.s.} \exp \left\{ -\frac{E_i}{k_B T_e} \right\}. \quad (29)$$

Here, the parameter

$$\bar{C} = S T \frac{hc}{4\pi\lambda} 2R q_0 \frac{A_{ij}}{\sum_j A_{ij}} \quad (30)$$

gathers the various constants and additionally accounts for the sensitivity S of the spectrometer and the transmission T of the various optic components involved. The strong dependencies on the electron density n_0 and the electron temperature T_e have been explicitly separated in Eq. (29). Consequently, the parameter \bar{C} is nearly constant with only a weak dependence on the electron temperature through the coefficient q_0 . Then, within this somewhat simplified model, \bar{C} is expected to vary slightly with the pressure and to be independent of the RF power. The value of \bar{C} depends weakly also on the power and the distance from the electrode via the contribution of non-linear processes, such as step-wise and cascade excitation, as well as depletion of the tungsten atoms through ionization. However, these processes have mostly a perturbative effect and are neglected in the following analysis.

For better reliability, the analysis has been performed using several different transitions of the tungsten atom. The parameters of these transitions are listed in Table V, and Fig. 12 presents their Grotrian diagram. The transitions are selected based on how well they could be resolved by the spectrometer and the absence of unresolved transitions from the other species present in the plasma (Ar I, Ar II, W II). All of the considered transitions exhibit the same trends, and here only results from the transition at $\lambda = 498.3$ nm will be shown as an illustration for the analysis. This transition is probably also the most suitable one, i.e., best fulfills the assumptions in the analysis due to the strong coupling of its upper level to the ground state of the tungsten atom (large branching ratio of the upper level of 79%). The transition is marked in Table V and in Fig. 12.

TABLE V. Transition wavelength λ , branching ratio $B_r = A_{ij} / \sum_j A_{ij}$ as well as energy of the upper E_u and the lower E_l level of the tungsten lines considered in this study. The data are taken from the NIST database.⁶⁶ Boldface indicates the 498.3 nm transition results.

λ (nm)	400.9	498.3	501.5	505.3	505.5	522.5	543.5	551.5
B_r	0.99	0.79	0.98	0.52	1.0	0.36	0.17	0.20
E_l (eV)	0.37	0	0.6	0.21	0.21	0.6	0.21	0.41
E_u (eV)	3.46	2.49	3.07	2.66	2.66	2.97	2.49	2.66

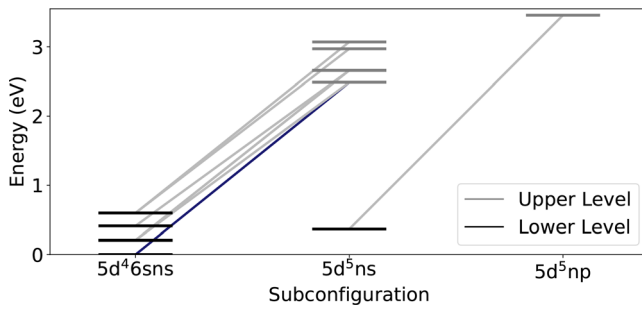


FIG. 12. Grotrian diagram for the energy levels of the investigated transitions of tungsten. The transitions are indicated by a line, which connects the upper and the lower level.

B. Tungsten density

The tungsten density $n_{W,g.s.}$ in Eq. (29) is related to the flux of the sputtered atoms:

$$\Gamma_W = n_{W,g.s.} v_n, \quad (31)$$

where v_n denotes the average velocity normal to the surface. Here, it is assumed that all sputtered atoms are in their ground state.⁶⁷ Further assumption is for an infinitely large plane with the sputtered flux having only a component in the normal direction. This is justified by the dimensions of the biased electrode relative to the distance at which the spectra are collected together with the relatively low pressure range and large mean free paths of the sputtered material. The average velocity v_\perp of the sputtered atoms is calculated with the use of the Thompson distribution \tilde{F}_v :

$$v_n = \frac{2}{3} \int_0^{v_{\max}} v \tilde{F}_v(v) dv. \quad (32)$$

The numerical coefficient accounts for the angular distribution of the sputtered particles and their maximal velocity v_{\max} as well as the distribution itself depend on the energy of the incoming ions E_{kin,Ar^+} . The detailed derivation can be found in the [Appendix](#).

Finally, the density of the sputtered tungsten atoms is related to the plasma density n_0 in front of the electrode by substituting Eq. (31) into Eq. (24):

$$n_{W,g.s.} = Y n_0 \frac{u_B}{v_n}. \quad (33)$$

This permits its calculation from the measured values of the plasma parameters. The resulting values for the density of the sputtered material are in the same order of magnitude as the plasma density. An estimation shows that this does not change the overall ionization balance in the plasma.

C. Consistency of the experimental data

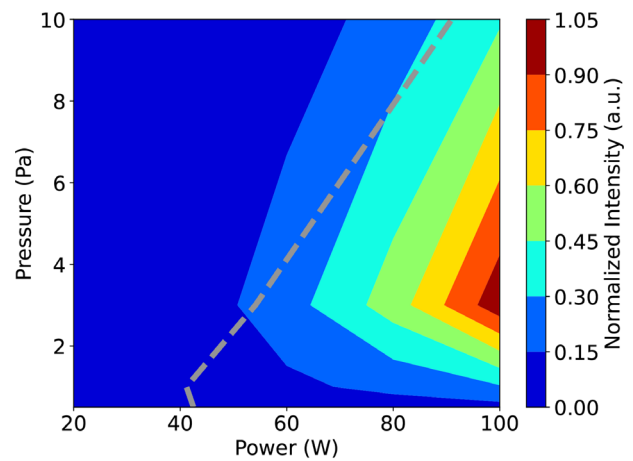
1. Intensity

The first comparison that can be made is between the measured intensity of the selected tungsten transition at 498.3 nm and the expected intensity estimated from the plasma parameters. The latter is obtained by inserting $n_{W,g.s.}$ from Eq. (33) into Eq. (29),

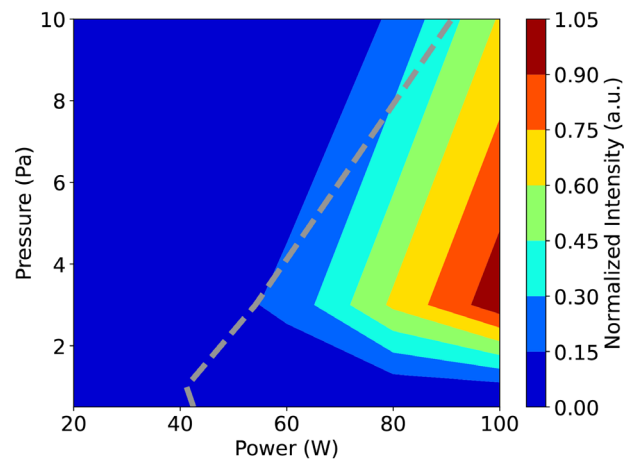
$$I_{i \rightarrow j} = Y \bar{C} \frac{n_0^2 u_B}{v_n} \exp \left\{ -\frac{E_i}{k_B T_e} \right\}. \quad (34)$$

For the purpose of the comparison, the parameter \bar{C} is set to a constant, i.e., only the relative variation of the intensity with the pressure and the power is compared. Overall, an excellent agreement is observed (Fig. 13). This confirms both the consistency of the various plasma parameters obtained by independent diagnostics and the validity of the approximations in the treatment.

The emission increases at each pressure with the power. This is due to the quadratic dependence of the intensity on the plasma density n_0 [Eq. (34)], which increases with the power (Fig. 3). The square root relation between n_0 and P [Eq. (10)] then translates into a linear dependence of the emission intensity on the power. Additionally,



(a) Simulated intensity



(b) Measured intensity

FIG. 13. Intensity of the tungsten transition at 498.3 nm (a) estimated with Eq. (34) using the measured plasma parameters and (b) measured at a distance of 0.5 cm to the electrode. The dashed curve marks the conditions at which the ion impact energy reaches 100 eV.

increasing the plasma density enlarges the self-bias at the electrode, which is critical for the sputtering process (Fig. 9).

At a constant power level, the intensity shows a maximum at 3 Pa. The formation of this maximum is due to a competition between the increase in n_0 as the pressure increases and the decrease in the energy of the impinging Ar^+ ions. The latter is signified by a curve that shows the conditions at which the ions reach a kinetic energy of 100 eV (Fig. 13). It is seen that at the higher pressures, this line marks the onset of the emission by the tungsten atoms. Below this energy, the sputter rate is insignificant and not enough tungsten atoms are present in the discharge for an appreciable emission intensity.

It would also be interesting to track the behavior of the emission of the tungsten ion W II. However, its strong lines are located in the spectral range 178–435 nm and are either not distinguishable from the Ar II lines or are outside the wavelengths accessible by the spectrometer.

2. Sputter yield

Finally, solving Eq. (34) for the sputter yield Y enables an investigation of the relative sputter yield by comparing it to the predictions of the empirical formula by Eckstein and Preuss.^{24–26} The expression for the sputter yield Y is then given by

$$Y = \frac{I_{i \rightarrow j}}{\bar{C}} \frac{v_n}{n_0^2 u_B \exp \left\{ -\frac{E_i}{k_B T_e} \right\}}. \quad (35)$$

Since the value of the factor \bar{C} has not been determined until, this provides only the relative shape of Y as a function of the energy of the impinging argon ions $E_{\text{kin}, \text{Ar}^+}$. To obtain the absolute values, the result of Eq. (35) with the plasma parameters for 100 W, i.e., the case with the highest intensity from the tungsten atoms and, thus, the highest signal-to-noise ratio, is scaled to the value of the empirical formula of Eckstein and Preuss.^{24–26} This provides the value of \bar{C} . The parameter is obtained in this way for each of the selected transitions at each investigated pressure and then used to calculate from them the absolute value of Y . The obtained values for Y are additionally averaged over the positions within the diagnostic volume (distance to the electrode of 0.5, 1.5, and 2.5 cm). All emission lines provide practically identical results, as illustrated in Fig. 14 for the case of 3 Pa. This verifies the assumption that the electron density has negligible influence on \bar{C} , as explained in Sec. IV A. Likewise, it can be inferred that either the Corona limit works reasonably well within the framework of this investigation or that the systematic error due to this approximation is mostly insensitive to the electron densities, which are typical for the discharge investigated here.

Applying this procedure for each of the investigated pressures and averaging over all eight transitions, which are shown in Fig. 14, finally provides benchmark values for the empirical formula of Eckstein and Preuss^{24–26} (Fig. 15). The results at 0.5 Pa are not included in the figure due to the weak emission intensity at this condition. This causes too large uncertainties that reduce the significance of the data.

Excellent agreement between the empirical formula and the experimental results is obtained. Some discrepancy at lower ion impact energies (below 100 eV) could be speculated. However, this could also be a result of the overestimation of the ion energy for the data at 10 Pa. Furthermore, the results are within the experimental uncertainty. Note

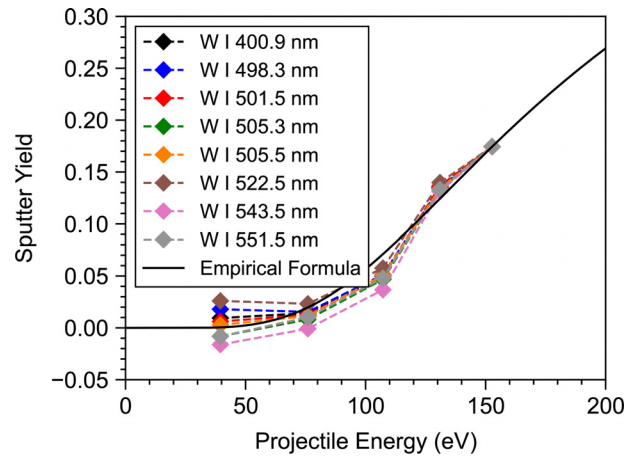


FIG. 14. The results of Eq. (35) for the different transitions, listed in Table V for a discharge at a pressure of 3 Pa and various RF power levels. The values of the corresponding coefficients \bar{C} are obtained through scaling to the empirical rate of Eckstein and Preuss^{24–26} for the case of 100 W (highest projectile energy).

that many of the data points lie near the onset of the sputter yield curve, i.e., the sputtering under these conditions is a near-threshold process.

V. OUTLOOK

Beside removing the depositions, the cleaning process should not damage the mirror to preserve its optical properties. One such solution for removing Be and BeO layers from the mirror is an RF discharge in deuterium.¹¹ Unlike beryllium depositions, tungsten is extremely weakly affected by bombardment with deuterium ions due to the high threshold energy of $E_{\text{th}} \approx 229$ eV.²⁵

RF discharges in argon or neon atmospheres should allow the removal also of the tungsten depositions while keeping the damage to the mirror at an acceptable level.¹³ At present, rhodium has been chosen as the material for the first core CXRS mirror.^{3,68,69} A simple estimation for the extent to which the RF discharge will affect the various

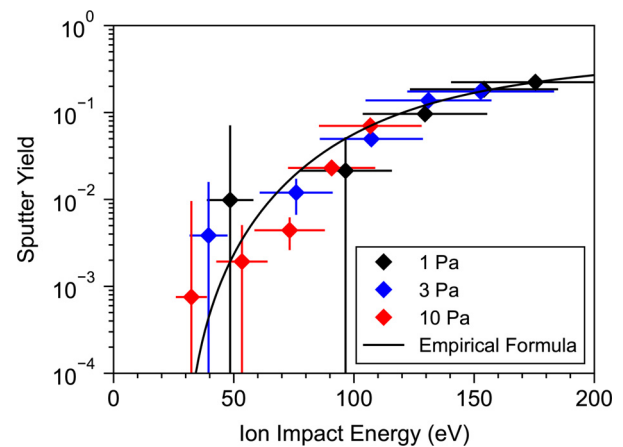


FIG. 15. Comparison of the sputter yield obtained through Eq. (35) with the empirical prediction of Eckstein and Preuss.^{24–26}

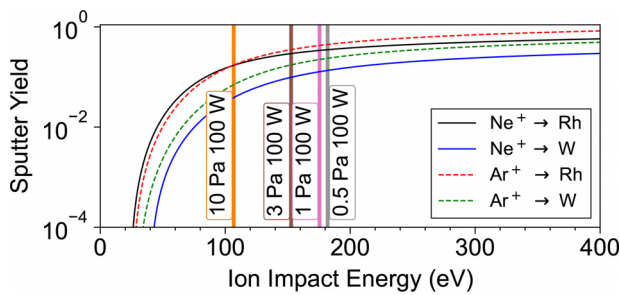


FIG. 16. Sputter yield of Rh and W by normally incident Ne^+ and Ar^+ .

materials (contaminating depositions and mirror crystal) can be obtained from their sputter yields. Figure 16 presents the sputter yields for Rh and W by Ne^+ and Ar^+ using the empirical formula of Eckstein and Preuss.^{24–26} Note that this estimation is likely only a crude simplification since preferential sputtering will occur.^{70,71} From these two gases, argon is likely the better option due to a more favorable removal rate of tungsten compared to the sputtering of the mirror material (rhodium).

An admixture of hydrogen or deuterium should make it possible to adjust the cleaning rate while providing also a constant sputter yield of about 0.02 (for ion energies in the range of 50–400 eV) for beryllium coverage.²⁵ Furthermore, a gas composition consisting of hydrogen and argon offers an “End-of-cleaning indicator,” such as DSRM, where the mirror reflectivity can be monitored by measuring the wings of the Balmer- α line.

VI. CONCLUSION

In this work, the various aspects of sputtering of tungsten in a high-frequency (60 MHz) capacitive discharge in argon have been investigated. Pressures in the range 0.5–10 Pa and power levels of 20 W–100 W have been considered. The biased electrode had the dimensions of the metallic mirror for diagnostics of the plasma in ITER since the study is motivated by the prospect of using such low-pressure RF discharges for mirror cleaning and recovery during the maintenance phases.

Various diagnostics provide a closed picture of the sputtering process. Using microwave interferometry in a combination with a Langmuir probe as well as optical emission spectroscopy with a collisional-radiative model for the argon atom the effective electron temperature and the plasma density are obtained. The probe measurements provide the radial profiles of the electron density and, with the help of an analytical model, some information about the radial distribution of the electron temperature. In contrast to that, the emission measurements grant insight into the axial variation of the plasma parameters. Both methods yield consistent values for the plasma parameters that also agree well with the general expectations for low-pressure RF capacitive discharges.

Measurements of the RF bias together with a model for the high-voltage sheath give the impact energy of the argon ions. Measurements of the emission intensity of the sputtered tungsten atoms together with a model estimation of their velocity give information about the flux of the sputtered particles.

The sputter rate reaches a maximum value of 2.6 Å/s at 3 Pa and 100 W. The obtained trends indicate that this value will further increase with the coupled RF power. The combination of all results via a simplified model permits also the estimation of the sputter yield, especially in the near-threshold region. Excellent agreement with the empirical formula of Eckstein and Preuss^{24–26} is obtained.

The general conclusion is that an RF discharge can be used for *in vacuo* cleaning of metallic mirrors in ITER and should be sufficient to achieve acceptable cleaning times even for “hard,” i.e., high-Z material depositions such as tungsten, provided the underlying mirror surface is not susceptible to damage under these conditions. A hydrogen-argon mixture with a high hydrogen content may be the best solution (Sec. IV). As an “End-of-cleaning indicator,” the reflectance of the mirror obtained by comparing blue and red-shifted emission from hydrogen atoms can be used, e.g., DSRM.

ACKNOWLEDGMENTS

This work has been carried out within the framework of the EUROfusion Consortium and has received funding from the Euratom Research and Training Program 2014–2018 and 2019–2020 under Grant Agreement No 633053. The views and opinions expressed herein do not necessarily reflect those of the European Commission.

AUTHOR DECLARATIONS

Conflict of Interest

The authors have no conflicts to disclose.

DATA AVAILABILITY

The data that support the findings of this study are available from the corresponding author upon reasonable request.

APPENDIX: VELOCITY NORMAL TO THE SURFACE

Here, the calculation of the velocity v_{\perp} of the sputtered atoms is explained in greater details and Eq. (32) is derived. The energy and angular distribution of the sputtered particles is usually well-described by the Thompson distribution:⁷²

$$F(E, \Omega) = C \frac{E}{(E + E_b)^{3-n}} \left(1 - \sqrt{\frac{E + E_b}{E_{\max} + E_b}} \right) \cos \theta, \quad (\text{A1})$$

where $E_b \approx 8.7$ eV is the surface binding energy of tungsten,²⁵ E_{\max} is the maximal kinetic energy of the particles leaving the surface, C is a normalization constant, and $n \approx 0$ is a scaling factor of the energy distribution.^{25,73} The particles leave the surface at an angle θ to its normal vector.

Generally, the angular distribution of the sputtered particles at low impact energies can be an under cosine ($\cos^b(\theta)$, $b < 1$) distribution, cosine ($b = 1$), over cosine ($b > 1$) or even a heart shaped distribution.⁷⁴ However, recently Ertmer *et al.*⁷³ obtained a reasonable agreement of the optical emission spectra of the sputtered tungsten atoms by Ar ion bombardment at impact energies of 70–150 eV when the angular distribution was assumed to be cosine.

Since the estimated ion impact energies in this work are in the same energy range, the treatment here also assumes a cosine angular distribution.

The maximum kinetic energy of the sputtered particles leaving the surface depends on the impact energy E_{imp} of the sputtering ions,⁷⁵

$$E_{\text{max}} = 4 \frac{M_1 \cdot M_2}{(M_1 + M_2)^2} E_{\text{imp}} - E_b, \quad (\text{A2})$$

where M_1 and M_2 are the masses of the sputtered and the sputtering particles, respectively. This relation explains the presence of a threshold for the sputtering process. For the sputtering to be possible ($E_{\text{max}} \geq 0$), the impinging ions need a minimal energy of

$$E_{\text{imp,min}} = \frac{1}{4} \frac{(M_1 + M_2)^2}{M_1 \cdot M_2} E_b. \quad (\text{A3})$$

For the Ar^+ -W system, this results in $E_{\text{imp,min}} = 14.8 \text{ eV}$, which is reasonably close to the actual value of about 27 eV .²⁵ The difference is due to the mechanism for sputtering—the impinging ions have to experience one collision in the crystal grid before an atom can be knocked out.

The velocity v_{\perp} is obtained from

$$v_n = \langle v \cos \theta \rangle = \iint v \cos \theta \tilde{F}(v, \Omega) dv d\Omega, \quad (\text{A4})$$

where $\tilde{F}(v, \Omega) = \tilde{F}(v) \pi^{-1} \cos \theta$ with

$$\tilde{F}_v(v) = C_v \frac{\frac{1}{2} M_1^2 v^3}{\left(\frac{1}{2} M_1 v^2 + E_b\right)^{3-n}} \left(1 - \sqrt{\frac{\frac{1}{2} M_1 v^2 + E_b}{\frac{1}{2} M_1 v_{\text{max}}^2 + E_b}}\right), \quad (\text{A5})$$

the velocity Thompson distribution.⁷⁶ The normalization constant is $C = C_v \pi^{-1}$ and C_v is determined from the condition,

$$\int_0^{v_{\text{max}}} \tilde{F}(v) dv = 1. \quad (\text{A6})$$

The maximum velocity is given by

$$v_{\text{max}} = \sqrt{\frac{2E_{\text{max}}}{M_1}}. \quad (\text{A7})$$

The integration over the solid angle in Eq. (A4) can be performed explicitly. This gives a numerical factor of $2/3$:

$$2\pi \int_0^{\pi/2} \frac{1}{\pi} \cos^2 \theta \sin \theta d\theta = \frac{2}{3}. \quad (\text{A8})$$

The limits of integration take into account that the particles are ejected only into a half-sphere in front of the surface ($0 \leq \theta \leq \pi/2$). Finally, the velocity v_{\perp} is obtained as

$$v_n = \frac{2}{3} \int_0^{v_{\text{max}}} v \tilde{F}_v(v) dv, \quad (\text{A9})$$

which is Eq. (32). The integration over the velocity has to be performed numerically, since no closed form for the integral exists.

REFERENCES

- ¹G. A. Naylor, R. Scannell, M. Beurskens, M. J. Walsh, I. Pastor, A. J. H. Donné, B. Snijders, W. Biel, B. Meszaros, L. Giudicotti, R. Pasqualotto, and L. Marot, "The ITER Thomson scattering core LIDAR diagnostic," *J. Instrum.* **7**, C03043 (2012).
- ²A. V. Gorbunov, E. E. Mukhin, E. B. Berik, K. Vukolov, V. S. Lisitsa, A. S. Kukushkin, M. G. Levashova, R. Barnsley, G. Vayakis, and M. J. Walsh, "Laser-induced fluorescence for ITER divertor plasma," *Fusion Eng. Des.* **123**, 695–698 (2017).
- ³Ph. Mertens, R. Boman, S. Dickheuer, Y. Krasikov, A. Krimmer, D. Leichtle, K. Liegeois, C. Linsmeier, A. Litnovsky, O. Marchuk, M. Rasinski, and M. De Bock, "On the use of rhodium mirrors for optical diagnostics in ITER," *Fusion Eng. Des.* **146**, 2514–2518 (2019).
- ⁴F. Romanelli, "Overview of the JET results with the ITER-like wall," *Nucl. Fusion* **53**, 104002 (2013).
- ⁵S. Brezinsek, A. Kirschner, M. Mayer, A. Baron-Wiechec, I. Borodkina, D. Borodin, I. Coffey, J. Coenen, N. den Harder, A. Eksaeva, C. Guillemaut, K. Heinola, A. Huber, V. Huber, M. Imrisek, S. Jachmich, E. Pawelec, M. Rubel, S. Krat, G. Sergienko, G. F. Matthews, A. G. Meigs, S. Wiesen, and A. Widdowson, "Erosion, screening, and migration of tungsten in the JET divertor," *Nucl. Fusion* **59**, 096035 (2019).
- ⁶V. Kotov, "Engineering estimates of impurity fluxes on the ITER port plugs," *Nucl. Fusion* **56**, 106027 (2016).
- ⁷D. Ivanova, M. Rubel, A. Widdowson, P. Petersson, J. Likonen, L. Marot, E. Alves, A. Garcia-Carrasco, and G. Pintsuk, "An overview of the comprehensive First Mirror Test in JET with ITER-like wall," *Phys. Scr.* **T159**, 014011 (2014).
- ⁸S. Ertmer, O. Marchuk, S. Dickheuer, S. Heuer, Ph. Mertens, M. Rasinski, B. Göths, S. Brezinsek, A. Houben, C. Linsmeier, and A. Kreter, "Monitoring removal of W layer from Ag substrate using Balmer- α emission of backscattered hydrogen atoms in low density gas discharge," *Acta Phys. Pol., A* **138**, 643–649 (2020).
- ⁹A. J. Stonehouse, "Physics and chemistry of beryllium," *J. Vac. Sci. Technol. A* **4**, 1163–1170 (1986).
- ¹⁰P. Chabert, Ts. V. Tsankov, and U. Czarnetzki, "Foundations of capacitive and inductive radio-frequency discharges," *Plasma Sources Sci. Technol.* **30**, 024001 (2021).
- ¹¹A. G. Razdobarin, A. M. Dmitriev, A. N. Bazhenov, I. M. Bukreev, M. M. Kochergin, A. N. Koval, G. S. Kurskiev, A. E. Litvinov, S. V. Masyukovich, E. E. Mukhin, D. S. Samsonov, V. V. Semenov, S. Tolstyakov, P. Andrew, V. L. Bukhovets, A. E. Gorodetsky, A. V. Markin, A. P. Zakharov, R. Zalavutdinov, P. V. Chernakov, T. V. Chernozumskaya, A. A. Kobelev, I. V. Miroshnikov, and A. S. Smirnov, "RF discharge for in situ mirror surface recovery in ITER," *Nucl. Fusion* **55**, 093022 (2015).
- ¹²L. Moser, R. Steiner, F. Leipold, R. Reichle, L. Marot, and E. Meyer, "Plasma cleaning of ITER First Mirrors in magnetic field," *J. Nucl. Mater.* **463**, 940–943 (2015).
- ¹³L. Moser, L. Marot, B. Eren, R. Steiner, D. Mathys, F. Leipold, R. Reichle, and E. Meyer, "Towards plasma cleaning of ITER first mirrors," *Nucl. Fusion* **55**, 063020 (2015).
- ¹⁴R. Yan, L. Moser, B. Wang, J. Peng, C. Vorpahl, F. Leipold, R. Reichle, R. Ding, J. Chen, L. Mu, R. Steiner, E. Meyer, M. Zhao, J. Wu, and L. Marot, "Plasma cleaning of ITER edge Thomson scattering mock-up mirror in the EAST tokamak," *Nucl. Fusion* **58**, 026008 (2018).
- ¹⁵F. Leipold, R. Reichle, C. Vorpahl, E. E. Mukhin, A. M. Dmitriev, A. G. Razdobarin, D. S. Samsonov, L. Marot, L. Moser, R. Steiner, and E. Meyer, "Cleaning of first mirrors in ITER by means of radio frequency discharges," *Rev. Sci. Instrum.* **87**, 11D439 (2016).
- ¹⁶A. M. Dmitriev, N. A. Babinov, A. N. Bazhenov, I. M. Bukreev, D. I. Elets, V. V. Filimonov, A. N. Koval, G. S. Kueskiev, A. E. Litvinov, E. E. Mikhin, A. G. Razdobarin, D. S. Samsonov, V. A. Senitchenkov, V. A. Solovei, I. B. Terechenko, Y. Tolstyakov, L. A. Varshavchik, P. V. Chernakov, Al. P. Chernakov, A. Chernakov, S. N. Tugarionov, P. A. Shigin, F. Leipold, R. Reichle, M. Walsh, and A. Pflug, "RF plasma cleaning of water-cooled mirror

- equipped with notch filter based on shorted $\lambda/4$ line," *Fusion Eng. Des.* **146**, 1390–1393 (2019).
- ¹⁷D. Eremin, S. Bienholz, D. Szeremley, J. Trieschmann, S. Ries, P. Awakowicz, T. Mussenbrock, and R. P. Brinkmann, "On the physics of a large CCP discharge," *Plasma Sources Sci. Technol.* **25**, 025020 (2016).
 - ¹⁸A. Messiaen, R. Koch, R. R. Weynants, P. Dumortier, F. Louche, R. Maggiore, and D. Milanesio, "Performance of the ITER ICRH system as expected from TOPICA and ANTITER II modelling," *Nucl. Fusion* **50**, 025026 (2010).
 - ¹⁹E. E. Mukhin, V. V. Semenov, A. G. Razdobarin, Y. Tolstyakov, M. M. Kochergin, G. S. Kurskiev, K. A. Podushnikova, S. V. Masyukevich, D. A. Kirilenko, A. A. Sitnikova, P. V. Chernakov, A. E. Gorodetsky, V. L. Bukhovets, K. Zalavutdinov, A. P. Zakharov, I. I. Arkhipov, Y. Khimich, D. B. Nikitin, V. N. Gorshkov, A. S. Smirnov, T. V. Chernozumskaja, E. M. Khilkevitch, S. V. Bulovich, V. S. Voitsenya, V. N. Bondarenko, V. G. Konovalov, I. V. Ryzhkov, O. M. Nekhaieva, O. A. Skorik, Y. Vukolov, V. I. Khripunov, and P. Andrew, "First mirrors in ITER: Material choice and deposition prevention/cleaning techniques," *Nucl. Fusion* **52**, 013017 (2012).
 - ²⁰D. Reiter, M. Baelmans, and P. Börner, "The EIRENE and B2-EIRENE Codes," *Fusion Sci. Technol.* **47**, 172–186 (2005).
 - ²¹A. Kirschner, V. Philipps, J. Winter, and U. Kögler, "Simulation of the plasma-wall interaction in a tokamak with the Monte Carlo code ERO-TEXTOR," *Nucl. Fusion* **40**, 989–1001 (2000).
 - ²²J. Romazanov, D. Borodin, A. Kirschner, S. Brezinsek, S. Silburn, A. Huber, V. Huber, H. Bufferand, M. Firdaouss, D. Brömmel, B. Steinbusch, P. Gibbon, A. Lasa, I. Borodkina, A. Eksaeva, and Ch. Linsmeier, "First ERO2.0 modeling of Be erosion and non-local transport in JET ITER-like wall," *Phys. Scr.* **T170**, 014018 (2017).
 - ²³A. Kreter, C. Brandt, A. Huber, S. Kraus, S. Möller, M. Reinhart, B. Schweer, G. Sergienko, and B. Unterberg, "Linear plasma device PSI-2 for plasma-material interaction studies," *Fusion Sci. Technol.* **68**, 8–14 (2015).
 - ²⁴W. Eckstein and R. Preuss, "New fit formulae for the sputtering yield," *J. Nucl. Mater.* **320**, 209–213 (2003).
 - ²⁵R. Behrisch and W. Eckstein, "Sputtering by particle bombardment: Experiments and computer calculations from threshold to MeV energies," in *Topics in Applied Physics*, edited by R. Behrisch and W. Eckstein (Springer, Berlin, 2007), Vol. 110, pp. 0303–4216.
 - ²⁶W. Eckstein, "Sputtering yields," *Vacuum* **82**, 930–934 (2008).
 - ²⁷B. G. Heil, U. Czarnetzki, R. P. Brinkmann, and T. Mussenbrock, "On the possibility of making a geometrically symmetric RF-CCP discharge electrically asymmetric," *J. Phys. D* **41**, 165202 (2008).
 - ²⁸O. Tudisco, A. Lucca Fabris, C. Falcetta, L. Accatino, R. de Angelis, M. Manente, F. Ferri, M. Florean, C. Neri, C. Mazzotta, D. Pavarin, F. Pollastrone, G. Rocchi, A. Selmo, L. Tasinato, F. Trezzolani, and A. A. Tuccillo, "A microwave interferometer for small and tenuous plasma density measurements," *Rev. Sci. Instrum.* **84**, 033505 (2013).
 - ²⁹J. E. Allen, R. L. F. Boyd, and P. Reynolds, "The collection of positive ions by a probe immersed in a plasma," *Proc. Phys. Soc. Sect. B* **70**, 297–304 (1957).
 - ³⁰F. F. Chen, "Langmuir probes in RF plasma: Surprising validity of OML theory," *Plasma Sources Sci. Technol.* **18**, 035012 (2009).
 - ³¹H. M. Mott-Smith and I. Langmuir, "The theory of collectors in gaseous discharges," *Phys. Rev.* **28**, 727–763 (1926).
 - ³²F. F. Chen, "Langmuir probe analysis for high density plasmas," *Phys. Plasmas* **8**, 3029–3041 (2001).
 - ³³M. A. Lieberman and A. J. Lichtenberg, *Principles of Plasma Discharges and Materials Processing*, 2nd ed. (Wiley-Interscience, Hoboken, NJ, 2005).
 - ³⁴S. Iordanova and I. Koleva, "Optical emission spectroscopy diagnostics of inductively-driven plasmas in argon gas at low pressures," *Spectrochim. Acta Part B* **62**, 344–356 (2007).
 - ³⁵D. L. Crintea, U. Czarnetzki, S. Iordanova, I. Koleva, and D. Luggenhölscher, "Plasma diagnostics by optical emission spectroscopy on argon and comparison with Thomson scattering," *J. Phys. D* **42**, 045208 (2009).
 - ³⁶X.-M. Zhu and Y.-K. Pu, "A simple collisional-radiative model for low-temperature argon discharges with pressure ranging from 1 Pa to atmospheric pressure: Kinetics of Paschen 1s and 2p levels," *J. Phys. D* **43**, 015204 (2010).
 - ³⁷A. R. Gizzatullin, Y. O. Zhelonkin, E. F. Voznesencky, and A. R. Gizzatullin, "Application of argon collisional-radiative model for inductive RF discharge research," *J. Phys.* **1328**, 012025 (2019).
 - ³⁸S. Siepa, S. Danko, Ts. V. Tsankov, T. Mussenbrock, and U. Czarnetzki, "On the OES line-ratio technique in argon and argon-containing plasmas," *J. Phys. D* **47**, 445201 (2014).
 - ³⁹S. Siepa, "Global collisional-radiative model for optical emission spectroscopy of argon and argon-containing plasmas," Ph.D. thesis (Ruhr-Universität Bochum, Bochum, 2017), available at <https://hss-opus.ub.ruhr-uni-bochum.de/opus4/frontdoor/index/index/docId/5354>.
 - ⁴⁰A. K. Bhatia and S. O. Kastner, "Doppler-profile escape factors and escape probabilities for the cylinder and hemisphere," *J. Quant. Spectrosc. Radiat. Transf.* **58**, 347–354 (1997).
 - ⁴¹A. Greiche, W. Biel, O. Marchuk, and R. Burhenn, "Absolute intensity calibration of the Wendelstein 7-X high efficiency extreme ultraviolet overview spectrometer system," *Rev. Sci. Instrum.* **79**, 093504 (2008).
 - ⁴²N. Bibinov, H. Halfmann, P. Awakowicz, and K. Wiesemann, "Relative and absolute intensity calibrations of a modern broadband Echelle spectrometer," *Meas. Sci. Technol.* **18**, 1327–1337 (2007).
 - ⁴³Q. Xiong, A. Y. Nikiforov, M. Á. González, C. Leys, and X. P. Lu, "Characterization of an atmospheric helium plasma jet by relative and absolute optical emission spectroscopy," *Plasma Sources Sci. Technol.* **22**, 015011 (2013).
 - ⁴⁴G. F. Karabadzak, Y.-h. Chiu, and R. A. Dressler, "Passive optical diagnostic of Xe propelled Hall thrusters. II. Collisional-radiative model," *J. Appl. Phys.* **99**, 113305 (2006).
 - ⁴⁵M. Griener, J. M. Muñoz Burgos, M. Cavedon, G. Birkenmeier, R. Dux, B. Kurzan, O. Schmitz, B. Siegl, U. Stroth, E. Viezzer, and E. Wolfrum, "Qualification and implementation of line ratio spectroscopy on helium as plasma edge diagnostic at ASDEX Upgrade," *Plasma Phys. Controlled Fusion* **60**, 025008 (2018).
 - ⁴⁶K. Makasheva and A. Shivarova, "Surface-wave-produced plasmas in a diffusion-controlled regime," *Phys. Plasmas* **8**, 836–845 (2001).
 - ⁴⁷E. W. McDaniel and E. A. Mason, *The mobility and diffusion of ions in gases: A Wiley-Interscience Publication* (Wiley, New York, 1973).
 - ⁴⁸Phelps database, see www.lxcat.net (2021).
 - ⁴⁹G. J. M. Hagelaar and L. C. Pitchford, "Solving the Boltzmann equation to obtain electron transport coefficients and rate coefficients for fluid models," *Plasma Sources Sci. Technol.* **14**, 722–733 (2005).
 - ⁵⁰V. A. Godyak, "Statistical heating of electrons at an oscillating plasma boundary," *Sov. Phys.-Tech. Phys. (Engl. Transl.)* **16**(7), 1073–1076 (1972).
 - ⁵¹V. A. Godyak and R. B. Piejak, "Abnormally low electron energy and heating-mode transition in a low-pressure argon RF discharge at 13.56 MHz," *Phys. Rev. Lett.* **65**, 996–999 (1990).
 - ⁵²J. Schulze, B. G. Heil, D. Luggenhölscher, T. Mussenbrock, R. P. Brinkmann, and U. Czarnetzki, "Electron beams in asymmetric capacitively coupled radio frequency discharges at low pressures," *J. Phys. D* **41**, 042003 (2008).
 - ⁵³E. Kawamura, V. Vahedi, M. A. Lieberman, and C. K. Birdsall, "Ion energy distributions in rf sheaths; review, analysis and simulation," *Plasma Sources Sci. Technol.* **8**, R45–R64 (1999).
 - ⁵⁴U. Czarnetzki, "Analytical model for the radio-frequency sheath," *Phys. Rev. E* **88**, 063101 (2013).
 - ⁵⁵A. V. Phelps, "The application of scattering cross sections to ion flux models in discharge sheaths," *J. Appl. Phys.* **76**, 747–753 (1994).
 - ⁵⁶Y. Yamamura and H. Tawara, "Energy dependence of ion-induced sputtering yields from monatomic solids at normal incidence," *At. Data Nucl. Data Tables* **62**, 149–253 (1996).
 - ⁵⁷K. Sugiyama, K. Schmid, and W. Jacob, "Sputtering of iron, chromium and tungsten by energetic deuterium ion bombardment," *Nucl. Mater. Energy* **8**, 1–7 (2016).
 - ⁵⁸N. Greenwood and A. Earnshaw, *Chemistry of the Elements*, 2nd ed. (Elsevier-Butterworth-Heinemann, Amsterdam, 2010).
 - ⁵⁹O. Marchuk, C. Brandt, and A. A. Pospieszczyk, "Verfahren zur Bestimmung der Oberflächeneigenschaften von Targets," German patent DE102016002270B3 (10 August 2017).
 - ⁶⁰O. Marchuk, C. Brandt, A. Pospieszczyk, M. Reinhart, S. Brezinsek, B. Unterberg, and S. Dickheuer, "Emission of fast hydrogen atoms at a plasma-solid interface in a low density plasma containing noble gases," *J. Phys. B* **51**, 025702 (2018).

- ⁶¹S. Dickheuer, O. Marchuk, C. Brandt, A. Pospieszczyk, A. Gorlaev, M. Ialovega, B. Göths, Y. Krasikov, A. Krimmer, Ph. Mertens, and A. Kreter, "In situ measurements of the spectral reflectance of metallic mirrors at the H_{α} line in a low density Ar-H plasma," *Rev. Sci. Instrum.* **89**, 063112 (2018).
- ⁶²G. Drake, *Springer Handbook of Atomic, Molecular, and Optical Physics* (Springer Science + Business Media Inc., New York, 2006).
- ⁶³Z. W. Cheng, X. M. Zhu, F. X. Liu, and Y. K. Pu, "Determination of the rate coefficients of the electron-impact excitation from the metastable states to 2p states of argon by the emission line ratios in an afterglow plasma," *J. Phys. D* **47**, 275203 (2014).
- ⁶⁴Z. W. Cheng, X. M. Zhu, F. X. Liu, and Y. K. Pu, "Determination of the rate coefficient of the electron-impact excitation from the argon resonance states ($1s_2$ and $1s_4$) to 2p states by the emission line ratio in an afterglow plasma," *Plasma Sources Sci. Technol.* **24**, 025025 (2015).
- ⁶⁵Z. W. Cheng, X. M. Zhu, N. Sadeghi, X. M. Guo, F. X. Liu, and Y. K. Pu, "Measurement of the electron-impact excitation rate coefficients from argon 1s states to 3p states," *J. Phys. D* **48**, 285202 (2015).
- ⁶⁶A. Kramida and Y. Ralchenko, "NIST Atomic Spectra Database, NIST Standard Reference Database 78."
- ⁶⁷S. Ertmer, O. Marchuk, A. Pospieszczyk, A. Kreter, and S. Brezinsek, "Ground state population of sputtered tungsten atoms by peak emission analysis in PSI-2 argon plasmas," in *Conference Proceeding 45th EPS Conference on Plasma Physics* (European Physical Society, 2018), p. P5.1024, available at <http://ocs.ciemat.es/EPS2018PAP/pdf/P5.1024.pdf>.
- ⁶⁸A. Litnovsky, Y. Krasikov, M. Rasinski, A. Kreter, C. Linsmeier, Ph. Mertens, B. Unterberg, U. Breuer, and T. Wegener, "First direct comparative test of single crystal rhodium and molybdenum mirrors for ITER diagnostics," *Fusion Eng. Des.* **123**, 674–677 (2017).
- ⁶⁹Ph. Mertens, "The core-plasma CXRS diagnostic for ITER: An introduction to the current design," *J. Fusion Energy* **38**, 264–282 (2019).
- ⁷⁰R. Kelly, "An attempt to understand preferential sputtering," *Nucl. Instrum. Methods* **149**, 553–558 (1978).
- ⁷¹S. Berg and I. V. Katardjiev, "Preferential sputtering effects in thin film processing," *J. Vac. Sci. Technol. A* **17**, 1916–1925 (1999).
- ⁷²M. W. Thompson, "II. The energy spectrum of ejected atoms during the high energy sputtering of gold," *Philos. Mag.* **18**, 377–414 (1968).
- ⁷³S. Ertmer, O. Marchuk, S. Dickheuer, S. Brezinsek, P. Boerner, J. Schmitz, and A. Kreter, "Measurements of the energy distribution of W atoms sputtered by low energy Ar ions using high-resolution Doppler spectroscopy," *Plasma Phys. Controlled Fusion* **63**, 015008 (2020).
- ⁷⁴M. Stepanova and S. K. Dew, "Estimates of differential sputtering yields for deposition applications," *J. Vac. Sci. Technol. A* **19**, 2805 (2001).
- ⁷⁵J. B. Sanders, *On Penetration Depths and Collision Cascades in Solid Materials* (Proefschrift–Leiden, Rototype, Amsterdam, 1968).
- ⁷⁶M. W. Thompson, "The velocity distribution of sputtered atoms," *Nucl. Instrum. Methods Phys. Res. Sect. B* **18**, 411–429 (1986).
- ⁷⁷T. V. Tsankov and U. Czarnetzki, "Information hidden in the velocity distribution of ions and the exact kinetic Bohm criterion," *Plasma Sources Sci. Technol.* **26**(5), 055003 (2017).